

## LARGE SCALE EXTRAGALACTIC JETS IN THE *Chandra* ERA I: DATA REDUCTION AND ANALYSIS

F. MASSARO<sup>1</sup>, D. E. HARRIS<sup>1</sup>, C. C. CHEUNG<sup>2</sup>

*version November 1, 2018: fm*

### ABSTRACT

In this paper we report the first stages of an investigation into the X-ray properties of extragalactic jets. Our approach is to subject all sources for which X-ray emission has been detected by *Chandra* to uniform reduction procedures. Using *Chandra* archival data for 106 such sources, we measure X-ray fluxes in three bands and compare these to radio fluxes. We discuss the sample, the reduction methods, and present first results for the ratio of X-ray to radio flux for jet knots and hotspots. In particular, we apply statistical tests to various distributions of key observational parameters to evaluate differences between the different classes of sources. Subsequent papers will deal with various ramifications such as considerations of how well the observational data fulfill expectations of the different radiation processes proposed for the knots of FRI radio galaxies and quasars.

*Subject headings:* Galaxies: active — galaxies: jets — Radio continuum: galaxies — X-rays: galaxies  
— Radiation mechanisms: non-thermal — Relativistic processes.

### 1. INTRODUCTION

Over the past decade, *Chandra* observations of radio galaxies (RGs) and quasars (QSRs) have provided crucial clues to investigate the nature of their extended components (e.g., jets and hotspots). Since the *Chandra* discovery of X-ray emission in the 100 kpc radio jet of PKS 0637-752 (Schwartz et al. 2000), the number of sources with X-ray detected extended components has increased from a handful to more than 100. For these radio sources with extended components detected in the X-ray band, we compiled their observed parameters, aiming at developing a *classification criterion* for these extragalactic components, independent of their core properties, and only based on the different radiative processes proposed to interpret their X-ray emission.

In 1974, Fanaroff and Riley introduced a classification scheme for extragalactic radio sources. Investigating the complete sample of 3C sources (Mackay 1971), they chose two main classes noting that relative positions of regions of high and low surface brightness in the extended regions of extragalactic radio sources are correlated with their radio luminosities. In particular, they divided these radio sources into two classes using the ratio  $R_{FR}$  of the distance between the regions of highest surface brightness on opposite sides of the central galaxy and/or quasar, to the total extent of the source up to the lowest brightness contour in the radio map. Sources with  $R_{FR} \leq 0.5$  were placed in Class I (i.e., FRI) and sources with  $R_{FR} \geq 0.5$  in Class II (i.e., FR II). In particular, at radio frequencies, FR Is show surface brightness higher toward their cores while FR IIs toward their edges (Fanaroff & Riley 1974).

Fanaroff and Riley found that all sources with luminosity  $L_{178\text{MHz}} \leq 2 \times 10^{25} h_{100}^{-2} \text{ W Hz}^{-1} \text{ str}^{-1}$  were classified as Class I while the brighter sources all were Class II. This luminosity boundary between them is not very

sharp, and there is some overlap in the luminosities of sources classified as FRI or FR II on the basis of their structures.

Since the original work, the FR scheme remains successful in classifying RGs. Extending the FR morphological/radio luminosity classification to radio-loud sources in general, one needs to consider the source orientation with respect to the observer. Under such ‘unification schemes’ (Urry & Padovani 1995), all radio-loud QSRs are posited to be FR II RG’s observed at smaller angles to our line of sight (see also Barthel 1989). Orr & Browne (1982) introduced a sub-classification for QSRs distinguishing between core-dominated quasars (CDQ) and lobe-dominated quasars (LDQ), on the basis of the ratio between each source’s radio core flux relative to the extended one (see also Hine & Scheuer 1980; Hough & Readhead 1989). The most core-dominated sources have the largest such ratios presumably due to Doppler boosting of emission from a relativistic jet aligned most closely to our line of sight. However, this classification based on core-dominance is not as useful as the basic FRI/FR II distinction since the determining parameters are more strongly dependent on the angular resolution and frequency of a particular observation, nor is there an obvious correlation with radio luminosity or other primary observational parameter (e.g., Landt et al. 2006).

The radio to optical emission arising from extended components of RGs and QSRs is widely interpreted as synchrotron radiation by relativistic particles (e.g., Meisenheimer et al. 1989; Scarpa & Urry 2002; Sambruna et al. 2004), whereas the origin of X-ray emission in their components (i.e., knots in jets and hotspots) is still unclear, but certainly non-thermal (see Harris & Krawczynski 2002; Harris & Krawczynski 2006; Worrall 2009). The main dichotomy lies in which emission mechanism, synchrotron or inverse Compton (IC) scattering, dominates the X-ray emission of jets and hotspots. The former describes emission from low power jets, typically in

<sup>1</sup> Harvard - Smithsonian Astrophysical Observatory, 60 Garden Street, Cambridge, MA 02138, USA

<sup>2</sup> National Research Council Research Associate, National Academy of Sciences, Washington, DC 20001, resident at Naval Research Laboratory, Washington, DC 20375, USA

FRIs, while the latter provides an explanation for high power RGs (i.e., FR IIs) and QSRs (see e.g., Harris & Krawczynski 2006).

Over the past ten years, we have collected a sample of RGs and QSRs for which the X-ray emission associated with their radio jets or hotspots has been detected by *Chandra*. The main goal of this endeavor (hereinafter *XJET project*<sup>3</sup>) (Harris et al. 2010; Massaro et al. 2010a; Massaro et al. 2011a) is the development of a new classification criterion based not only on the radio morphology and power but also on the X-ray properties of these extended components. Our goal is to find criteria to distinguish between knots in jets and hotspots, both in RGs and QSRs, linked with the radiative process responsible for their X-ray emission. Here, we present the X-ray data reduction and analysis procedures together with some basic results. The current work (Paper I) represents our initial effort, and although we have not yet developed a new classification scheme as originally envisaged, we will explore additional lines of investigation in forthcoming works, such as including the information at optical frequencies to see if a more complete SED description will permit us a better differentiation of extragalactic jet components. In particular, the XJET project guidelines can be summarized as follows: in Paper II (Massaro et al. 2011b), we develop a statistical test for the IC/CMB model in QSR jets, while in Paper III (Massaro et al. 2011c), we plan to introduce the radio and X-ray emission from the cores as new parameters that could be used to classify RG and QSR jets and we will also provide measurements of the upper limits for the undetected X-ray components in our XJET sample, taking into account the *Chandra* sensitivity limits. In Paper IV (Harris et al. 2011), we will present a detailed comparison between the distributions of the observed parameters and the expectations of both analytical and numerical calculations for different radiative scenarios. Finally, the possible extension of the XJET project to the infrared and optical frequencies is already in progress.

Throughout, we assume a flat cosmology with  $H_0 = 72 \text{ km s}^{-1} \text{ Mpc}^{-1}$ ,  $\Omega_M = 0.26$  and  $\Omega_\Lambda = 0.74$  (Dunkley et al. 2009) and spectral indices,  $\alpha$ , are defined by flux density,  $S_\nu \propto \nu^{-\alpha}$ . Unless otherwise stated, we use cgs units.

## 2. THE XJET SAMPLE

The sample considered for our investigation consists of 106 radio sources with a published *Chandra* X-ray detection of a radio knot and/or hotspot, for a total of 236 components. The selected sample contains: 22 FR I RGs, 29 FR II RGs, 3 BL Lacs, and 52 QSRs (35 CDQs and 17 LDQs). In AGN unification schemes, QSRs and BL Lacs are broadly understood as FR IIs and FR Is, respectively, observed at smaller angles with respect to the line of sight (e.g., Urry & Padovani 1995; Landt et al. 2004).

The 236 components consist of 41 hotspots in FR II RGs and 21 in QSRs; 58 knots in FR I RGs, 22 in FR II RGs, 68 in CDQs, 19 in LDQs, and 7 in the BL Lacs. All these knots and hotspots have been classified on the basis of the radio morphology of their parent source, adopting the definition suggested by Leahy et al. (1997) for

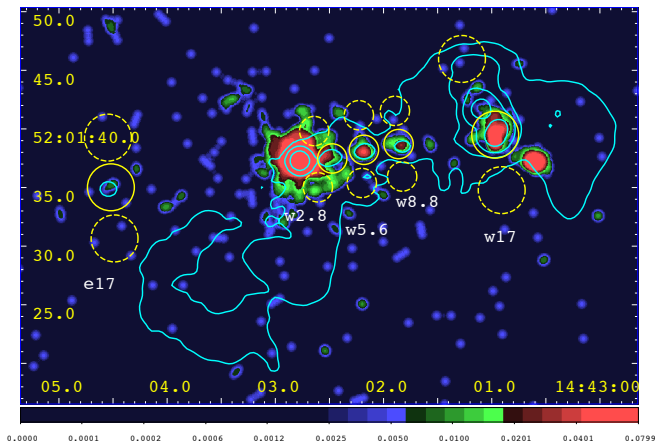


FIG. 1.— An X-ray image of 3C303 with radio contours (1.4 GHz) overlaid. The X-ray image is for the band 0.5-7 keV and has been smoothed with a Gaussian of FWHM=0.87". Radio contours start at 2 mJy/beam and increase by factors of 4. Photometric regions are shown in yellow, with background regions dashed. The labels are based on the cardinal direction from the nucleus and the distance in arcsec from the nucleus. Note the northern background circle for w17 is moved further north than usual so as to avoid the secondary hotspot. When a region is close to a bright nucleus, we deploy the background circles so as to lie at the same distance from the nucleus as the 'on' region (e.g. w2.8). The logarithmic scale of the X-ray brightness runs from 0.002 (black) to 0.08 (red) but the peak intensity is 6.29 counts per pixel. The pixel size in this image is 0.0615". Coordinates are in J2000.0 equinox.

the hotspots, i.e., brightness peaks which are neither the core nor a part of the jet, usually lying where the jet terminates, and considering all other discrete brightness enhancements as jet knots. Here, we did not investigate the extended radio/X-ray emission arising from lobes – the typically roughly symmetrical kpc-scale double radio structures lying on both sides of the host RG and/or QSR. The identification of BL Lacs have been adopted according to the ROMA BZCAT classification scheme<sup>4</sup> (Massaro et al. 2009a). Finally, we note that due to the small number of BL Lacs in our sample, and their limited number of components (i.e., only 7 out of 236), we did not consider the comparison between them class and the RGs or the QSRs.

The following conventions for the knots has been adopted for all the figures:

- FR I RGs = 'k1' (filled black squares)
- FR II RGs = 'k2' (filled red squares)
- CDQs = 'kqc' (filled green squares)
- LDQs = 'kql' (filled blue squares)

while we label hotspots as follows:

- FR II RGs = 'hs2' (open red circles)
- QSRs = 'hsq' (open blue circles)

We also introduce a nomenclature for indicating each component in every source. The name of each knot or hotspot is a combination of one letter indicating the orientation of the radio structure and one number indicating

<sup>3</sup> <http://hea-www.harvard.edu/XJET/>

<sup>4</sup> <http://www.asdc.asi.it/bzcat/>

TABLE 1  
THE BASIC PARAMETERS OF THE (00-08 H) SOURCES CONSIDERED IN THE XJET SAMPLE (SEE SECTION 2).

Name	Class	RA (J2000)	DEC (J2000)	z	$D_L$ [Mpc]	scale [kpc''']	$N_{H,Gal}$ [ $10^{20} \text{ cm}^{-2}$ ]	<i>Chandra</i> Obs ID	CFS	CFM	Ref.
3C 6.1	FR II	00 16 31.147	+79 16 49.88	0.8404	5297	7.58	15.5	3009	2.35	1.20	H04
3C 9	LDQ	00 20 25.220	+15 40 54.73	2.0120	15777	8.43	3.57	1595	1.22	1.04	1
3C 15	FR I	00 37 04.114	-01 09 08.46	0.0730	321	1.35	2.32	2178	1.14	1.02	2
3C 17	FR II	00 38 20.528	+02 07 40.49	0.2197	1066	3.47	1.99	9292	1.12	1.02	M09
NGC 315	FR I	00 57 48.891	+30 21 08.75	0.0165	70	0.33	5.83	4156	1.38	1.07	3
3C 31	FR I	01 07 24.961	+32 24 45.01	0.0167	71	0.33	5.36	2147	1.34	1.07	4
0106+013	CDQ	01 08 38.771	+01 35 00.31	2.0990	16626	8.39	2.42	9281	1.14	1.02	H11
3C 33	FR II	01 08 52.878	+13 20 14.38	0.0597	260	1.12	3.23	7200	1.20	1.05	5
3C 47	LDQ	01 36 24.423	+20 57 27.40	0.4250	2297	5.48	4.95	2129	1.30	1.06	H04
3C 52	FR II	01 48 28.909	+53 32 28.04	0.2854	1437	4.22	16.8	9296	2.49	1.23	M10
4C +35.03	FR I	02 09 38.553	+35 47 51.04	0.0369	158	0.71	6.16	856	1.40	1.08	W01
PKS 0208-512	CDQ	02 10 46.283	-51 01 02.95	0.9990	6575	7.98	1.84	4813	1.11	1.02	M05
3C 61.1	FR II	02 22 35.571	+86 19 06.38	0.1878	893	3.07	7.87	9297	1.53	1.10	M10
3C 66B	FR I	02 23 11.409	+42 59 31.25	0.0215	91	0.42	7.67	828	1.52	1.09	6
3C 83.1	FR I	03 18 15.669	+41 51 27.91	0.0251	107	0.49	13.4	3237	2.11	1.19	7
3C 105	FR II	04 07 16.453	+03 42 25.80	0.0890	396	1.62	11.5	9299	1.88	1.16	M10
PKS 0405-123	CDQ	04 07 48.432	-12 11 36.69	0.5740	3305	6.47	3.48	2131	1.22	1.05	S04
3C 109	FR II	04 13 40.349	+11 12 14.78	0.3056	1556	4.43	15.2	4005	2.30	1.21	H04
PKS 0413-210	CDQ	04 16 04.364	-20 56 27.70	0.8080	5043	7.48	2.49	3110	1.15	1.03	M05
3C 111	FR II	04 18 21.309	+38 01 36.28	0.0485	210	0.93	29.1	9279	4.30	1.40	H11
3C 120	FR I	04 33 11.098	+05 21 15.59	0.0330	141	0.64	10.6	3015	1.78	1.14	8
3C 123	FR II	04 37 04.367	+29 40 13.67	0.2177	1055	3.45	18.0	829	2.62	1.24	9
3C 129	FR I	04 49 09.072	+45 00 39.35	0.0208	88	0.41	59.6	2218	15.56	1.93	10
Pictor A	FR II	05 19 49.700	-45 46 44.50	0.0350	150	0.68	3.12	346	1.18	1.03	11
PKS 0521-365	BL	05 22 57.992	-36 27 30.62	0.0550	239	1.04	3.58	846	1.22	1.04	12
0529+075	CDQ	05 32 38.998	+07 32 43.31	1.2540	8745	8.35	17.1	9289	2.54	1.22	H11
PKS 0605-085	CDQ	06 07 59.700	-08 34 49.98	0.8700	5531	7.67	18.3	2132	2.64	1.25	S04
3C 173.1	FR II	07 09 18.187	+74 49 31.91	0.2920	1476	4.29	4.60	3053	1.29	1.06	H04
3C 179	LDQ	07 28 10.901	+67 48 47.70	0.8460	5341	7.60	4.38	2133	1.27	1.06	S02
B2 0738+313	CDQ	07 41 10.703	+31 12 00.23	0.6310	3712	6.77	4.32	377	1.27	1.06	13
3C 189	FR I	07 58 28.109	+37 47 11.79	0.0428	184	0.82	4.68	858	1.29	1.05	W01

Note: ‘CFS’ and ‘CFM’ correspond to the correction factor for the Galactic absorption in the soft and in the medium bands, respectively (see Section 3.3 for more details).

References: H04 (Hardcastle et al. 2004), (1) (Fabian et al. 2003a), (2) (Kataoka et al. 2003b), M09 (Massaro et al. 2009c), (3) (Worrall et al. 2003), (4) (Hardcastle et al. 2002a), H11 (Hogan et al. 2011), (5) (Kraft et al. 2007), M10 (Massaro et al. 2010b), W01 (Worrall et al. 2001), M05 (Marshall et al. 2005), (6) (Hardcastle et al. 2001b), (7) (Sun et al. 2005), S04 (Sambruna et al. 2004), (8) (Harris et al. 2004), (9) (Hardcastle et al. 2001a), (10) (Harris et al. 2002), (11) (Wilson et al. 2001), (12) (Birkinshaw et al. 2002), S02 (Sambruna et al. 2002), (13) (Siemiginowska et al. 2003a).

distance from the core in arcsec. The case of 3C 303 is shown as an example in Figure 1.

All the components identified in our analysis have been previously discovered as reported in the referenced papers (see Table 1, 2 and 3) with four exceptions, namely: n46.4 in 3C 109, n3.5, n5.6 in M 84 and w6.0 in 3C 280, that we detected because in this work we used *Chandra* observation with longer exposure than the previous ones. In Table 1, 2 and 3 we summarize the whole XJET sample and the main properties of the sources. We report the name, the source class (e.g., FR I, LDQ etc.), the radio coordinates adopted for the registration of the X-ray image (see Section 3 for details), the redshift ( $z$ ), and the corresponding scale (kpc''') and luminosity distance,  $D_L$  (Wright 2006)<sup>5</sup>, the Galactic absorption (Kalberla et al. 2005), the *Chandra* observation ID in which the radio component is detected in the X-rays, and the correction factors computed to correct the X-ray fluxes for the Galactic absorption in the soft and the medium bands (see Section 3.3). In Figure 2, we show the

<sup>5</sup> For the 3 nearby objects (Centaurus A, M 87, M 84), distances from the literature are adopted in favor of those computed based on their redshifts.

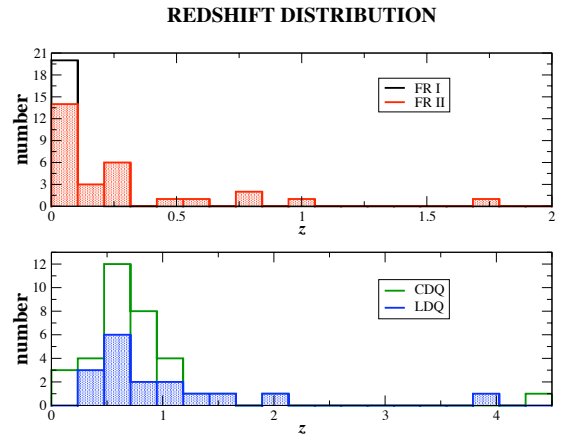


FIG. 2.— The redshift distributions for the RGs (upper panel) and QSRs (lower panel) in the XJET selected sample.

redshift distributions of RGs and QSRs in our selected sample. We show the plot of the X-ray count rate of each component vs. the redshift for both knots and hotspots

TABLE 2  
THE BASIC PARAMETERS OF THE (08-16 H) SOURCES CONSIDERED IN THE XJET SAMPLE (SEE SECTION 2).

Name	Class	RA (J2000)	DEC (J2000)	z	$D_L$ [Mpc]	scale [kpc/"]	$N_{H,Gal}$ [ $10^{20} \text{ cm}^{-2}$ ]	Chandra Obs ID	CFS	CFM	Ref.
0827+243	CDQ	08 30 52.086	+24 10 59.83	0.9390	6085	7.85	2.92	3047	1.17	1.04	14
4C +29.30	FR I	08 40 02.356	+29 49 02.49	0.0640	280	1.20	4.23	2135	1.27	1.05	S04
3C 207	LDQ	08 40 47.589	+13 12 23.59	0.6800	4071	6.99	4.27	2130	1.27	1.05	15
3C 212	LDQ	08 58 41.460	+14 09 44.79	1.0490	6991	8.07	3.79	434	1.23	1.04	16
PKS 0903-573	CDQ	09 04 53.184	-57 35 05.85	0.6950	4183	7.06	27.0	3113	3.99	1.38	M05
3C 219	FR II	09 21 08.620	+45 38 57.40	0.1744	823	2.89	1.35	827	1.08	1.02	17
PKS 0920-397	CDQ	09 22 46.413	-39 59 34.96	0.5910	3425	6.56	17.7	5732	2.58	1.24	M05
3C 227	FR II	09 47 45.140	+07 25 21.07	0.0861	383	1.57	2.11	6824	1.12	1.02	H07
Q 0957+561	LDQ	10 01 20.840	+55 53 49.56	1.4100	10129	8.46	0.93	362	1.05	1.01	18
4C +13.41	LDQ	10 07 26.099	+12 48 56.19	0.2408	1183	3.72	3.56	5606	1.23	1.03	19
PKS 1030-357	CDQ	10 33 07.660	-36 01 56.80	1.4550	10536	8.48	5.97	5730	1.39	1.08	M05
1045-188	CDQ	10 48 06.602	-19 09 35.97	0.5950	3454	6.58	3.38	9280	1.19	1.03	H11
PKS 1046-409	CDQ	10 48 38.275	-41 14 00.15	0.6200	3633	6.71	7.73	3116	1.52	1.09	M05
4C +20.24	LDQ	10 58 17.870	+19 51 50.86	1.1100	7504	8.17	1.69	7795	1.11	1.02	20
3C 254	LDQ	11 14 38.725	+40 37 20.29	0.7340	4476	7.22	1.44	2209	1.09	1.02	D03
PKS 1127-145	CDQ	11 30 07.051	-14 49 27.41	1.1800	8102	8.27	3.39	5708	1.21	1.04	21
PKS 1136-135	LDQ	11 39 10.701	-13 50 43.41	0.5540	3165	6.35	3.31	3973	1.20	1.04	S02
3C 263	LDQ	11 39 57.023	+65 47 49.50	0.6563	3897	6.89	0.90	2126	1.05	1.01	H02
3C 264	FR I	11 45 05.008	+19 36 22.76	0.0217	92	0.43	1.83	4916	1.10	1.01	22
3C 265	FR II	11 45 28.959	+31 33 47.12	0.8110	5067	7.49	1.79	2984	1.11	1.02	23
4C +49.22	CDQ	11 53 24.407	+49 31 06.95	0.3340	1726	4.70	2.07	2139	1.13	1.02	S02
PKS 1202-262	CDQ	12 05 33.180	-26 34 04.00	0.7890	4896	7.42	7.72	4812	1.52	1.09	M05
3C 270	FR I	12 19 23.212	+05 49 31.08	0.0074	31	0.15	1.75	834	1.11	1.02	24
PG 1222+216	CDQ	12 24 54.458	+21 22 46.40	0.4320	2342	5.54	2.09	3049	1.13	1.02	J06
M 84	FR I	12 25 03.729	+12 53 13.20	0.0035	17	0.08	2.99	5908	1.18	1.04	25
3C 273	CDQ	12 29 06.704	+02 03 08.63	0.1583	739	2.67	1.67	4876	1.11	1.02	26
M 87	FR I	12 30 49.423	+12 23 28.05	0.0043	16	0.08	1.94	2707	1.11	1.02	27
PKS 1229-027	CDQ	12 32 00.018	-02 24 04.10	1.0450	6957	8.07	2.13	4841	1.13	1.02	28
3C 275.1	LDQ	12 43 57.676	+16 22 53.40	0.5550	3172	6.36	1.77	2096	1.11	1.02	C03
3C 280	FR II	12 56 57.201	+47 20 19.88	0.9960	6551	7.97	1.24	2210	1.08	1.02	D03
1317+520	CDQ	13 19 46.204	+51 48 05.77	1.0600	7083	8.09	1.32	3050	1.08	1.02	J06
3C 281	LDQ	13 07 53.925	+06 42 13.81	0.6020	3504	6.62	2.19	1593	1.02	1.12	C03
Centaurus A	FR I	13 25 27.616	-43 01 08.84	0.0018	3.8	0.02	8.09	8490	1.55	1.10	29
4C +65.15	LDQ	13 25 29.714	+65 15 13.16	1.6250	12096	8.51	1.91	7882	1.11	1.02	30
3C 287.1	FR II	13 32 53.257	+02 00 45.60	0.2156	1043	3.42	1.63	9309	1.11	1.02	M10
Centaurus B	FR I	13 46 49.036	-60 24 29.41	0.0130	55	0.26	105.0	3120	68.10	2.89	M05
4C +19.44	CDQ	13 57 04.438	+19 19 07.35	0.7200	4370	7.16	2.49	7302	1.15	1.03	S02
3C 294	FR II	14 06 44.069	+34 11 25.54	1.7860	13608	8.50	1.36	3207	1.09	1.02	31
3C 295	FR II	14 11 20.543	+52 12 09.88	0.4500	2460	5.67	1.34	2254	1.08	1.02	32
3C 296	FR I	14 16 52.953	+10 48 26.76	0.0237	101	0.47	1.92	3968	1.12	1.02	33
PKS 1421-490	LDQ	14 24 31.925	-49 13 54.77	0.6620	3939	6.91	15.7	5729	2.37	1.23	34
3C 303	FR I	14 43 02.777	+52 01 37.33	0.1410	651	2.42	1.71	1623	1.10	1.02	35
1508+572	CDQ	15 10 02.900	+57 02 44.00	4.3000	39725	6.86	1.57	2241	1.10	1.02	36
PKS 1510-089	CDQ	15 12 50.536	-09 05 59.73	0.3610	1892	4.95	6.89	2141	1.46	1.08	S04
3C 321	FR II	15 31 43.474	+24 04 19.02	0.0960	430	1.73	3.82	3138	1.24	1.04	H04

Note: 'CFS' and 'CFM' correspond to the correction factor for the Galactic absorption in the soft and in the medium bands, respectively (see Section 3.3 for more details).

References: (14) (Jorstad & Marscher 2004), S04 (Sambruna et al. 2004), (15) (Brunetti et al. 2002), (16) (Aldcroft et al. 2003), M10 (Massaro et al. 2010b), M05 (Marshall et al. 2005), (17) (Comastri et al. 2003), H07 (Hardcastle et al. 2007), (18) (Chartas et al. 2002), (19) (Miller et al. 2006), H11 (Hogan et al. 2011), (20) (Schwartz et al. 2006), D03 (Donahue et al. 2003), (21) (Siemiginowska et al. 2002), S02 (Sambruna et al. 2002), H02 (Hardcastle et al. 2002b), (22) (Perlman et al. 2010b), (23) (Bondi et al. 2004), (24) (Chiaberge et al. 2003), J06 (Jorstad & Marscher 2006), (25) (Finoguenov et al. 2008), (26) (Marshall et al. 2001), (27) (Marshall et al. 2002), (28) (Tavecchio et al. 2007), C03 (Crawford & Fabian 2003), (29) (Kraft et al. 2000), (30) (Miller & Brandt 2009), (31) (Fabian et al. 2003b), (32) (Harris et al. 2000), (33) (Hardcastle et al. 2005a), (34) (Gelbord et al. 2005), (35) (Kataoka et al. 2003a), (36) (Siemiginowska et al. 2003b), H04 (Hardcastle et al. 2004), S04 (Sambruna et al. 2004).

TABLE 3  
THE BASIC PARAMETERS OF THE (16-24 H) SOURCES CONSIDERED IN THE XJET SAMPLE (SEE SECTION 2).

Name	Class	RA (J2000)	DEC (J2000)	z	$D_L$ [Mpc]	scale [kpc/"]	$N_{H, Gal}$ [ $10^{20} \text{ cm}^{-2}$ ]	<i>Chandra</i> Obs ID	CFS	CFM	Ref.
3C 327	FR II	16 02 27.370	+01 57 56.24	0.1039	468	1.86	5.92	6841	1.38	1.06	H07
4C +00.58	FR I	16 06 12.687	+00 00 27.22	0.0590	257	1.11	7.14	10304	1.46	1.09	37
3C 330	FR II	16 09 34.930	+65 56 37.78	0.5500	3137	6.33	2.66	2127	1.16	1.03	H02
NGC 6251	FR I	16 32 31.981	+82 32 16.34	0.0249	106	0.49	5.57	4130	1.35	1.07	38
1642+690	CDQ	16 42 07.866	+68 56 39.75	0.7510	4605	7.28	5.15	2142	1.32	1.07	S04
3C 345	CDQ	16 42 58.810	+39 48 37.00	0.5940	3447	6.58	1.14	2143	1.08	1.02	S04
3C 346	FR I	16 43 48.613	+17 15 49.54	0.1610	753	2.71	5.07	3129	1.32	1.06	39
3C 349	FR II	16 59 28.893	+47 02 55.04	0.2050	986	3.29	1.88	9316	1.11	1.02	M10
3C 351	LDQ	17 04 41.417	+60 44 30.65	0.3720	1960	5.05	2.02	2128	1.12	1.02	H02
3C 353	FR II	17 20 28.168	-00 58 46.52	0.0304	130	0.59	9.37	7886	1.67	1.12	40
4C +62.29	LDQ	17 46 14.033	+62 26 54.77	3.8890	35233	7.15	3.09	4158	1.19	1.05	41
1800+440	CDQ	18 01 32.315	+44 04 21.83	0.6630	3946	6.92	3.14	9286	1.18	1.03	H11
3C 371	BL	18 06 50.671	+69 49 28.06	0.0510	221	0.97	4.16	2959	1.26	1.05	42
3C 380	CDQ	18 29 31.781	+48 44 46.17	0.6920	4160	7.05	5.78	3124	1.37	1.08	M05
3C 390.3	FR II	18 42 08.981	+79 46 17.21	0.0561	244	1.06	3.47	830	1.21	1.05	H07
1849+670	CDQ	18 49 16.072	+67 05 41.68	0.6570	3902	6.89	5.00	9291	1.31	1.05	H11
4C +73.18	CDQ	19 27 48.495	+73 58 01.57	0.3020	1535	4.39	7.15	2145	1.47	1.09	S04
3C 403	FR II	19 52 15.796	+02 30 24.39	0.0590	257	1.11	12.2	2968	1.96	1.17	43
Cygnus A	FR II	19 59 28.358	+40 44 02.09	0.0560	244	1.06	27.2	360	3.99	1.37	44
2007+777	BL	20 05 30.965	+77 52 43.21	0.3420	1775	4.78	8.35	5709	1.56	1.10	45
PKS 2101-490	CDQ	21 05 01.158	-48 48 46.52	0.0630	275	1.18	2.91	5731	1.18	1.04	M05
PKS 2153-69	FR II	21 57 06.035	-69 41 24.09	0.0283	121	0.55	2.64	1627	1.16	1.04	46
2155-152	CDQ	21 58 06.282	-15 01 09.32	0.6720	4012	6.96	3.59	9284	1.21	1.03	H11
PKS 2201+044	CDQ	22 04 17.630	+04 40 02.00	0.0270	115	0.53	4.35	2960	1.26	1.05	47
2209+080	CDQ	22 12 01.599	+08 19 16.44	0.4850	2692	5.92	5.58	3051	1.35	1.07	J06
2216-038	CDQ	22 18 52.038	-03 35 36.89	0.9010	5778	7.75	5.41	9285	1.34	1.06	H11
3C 445	FR II	22 23 49.548	-02 06 13.22	0.0562	244	1.06	4.49	7869	1.26	1.04	48
3C 452	FR II	22 45 48.771	+39 41 15.86	0.0811	359	1.49	9.64	2195	1.68	1.12	H04
3C 454.3	CDQ	22 53 57.748	+16 08 53.56	0.8590	5444	7.64	6.63	4843	1.44	1.08	M05
3C 465	FR I	23 38 29.383	+27 01 53.27	0.0293	125	0.57	4.82	4816	1.30	1.05	49

Note: ‘CFS’ and ‘CFM’ correspond to the correction factor for the Galactic absorption in the soft and in the medium bands, respectively (see Section 3.3 for more details).

References: H07 (Hardcastle et al. 2007), (37) (Hodges-Kluck et al. 2010), H02 (Hardcastle et al. 2002b), (38) (Evans et al. 2005), S04 (Sambruna et al. 2004), M10 (Massaro et al. 2010b), (39) (Worrall et al. 2005), (40) (Kataoka et al. 2008), (41) (Cheung et al. 2006), H11 (Hogan et al. 2011), (42) (Pesce et al. 2001), M05 (Marshall et al. 2005), H07 (Hardcastle et al. 2007), (43) (Kraft et al. 2005), (44) (Wilson et al. 2000), (45) (Sambruna et al. 2008), (46) (Ly et al. 2005), (47) (Sambruna et al. 2007), (48) (Perlman et al. 2010a), H04 (Hardcastle et al. 2004), (49) (Hardcastle et al. 2005b).

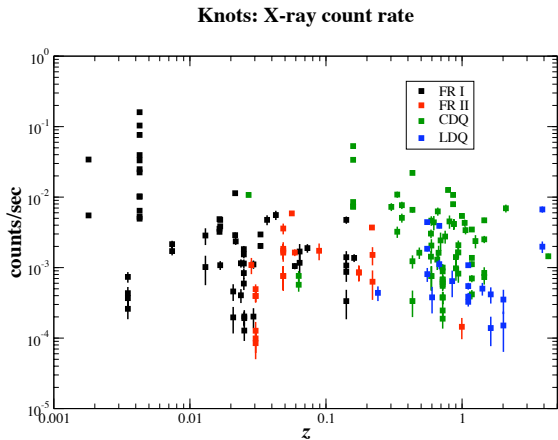


FIG. 3.— The X-ray count rate of knots in RGs and QSRs with respect to the redshift.

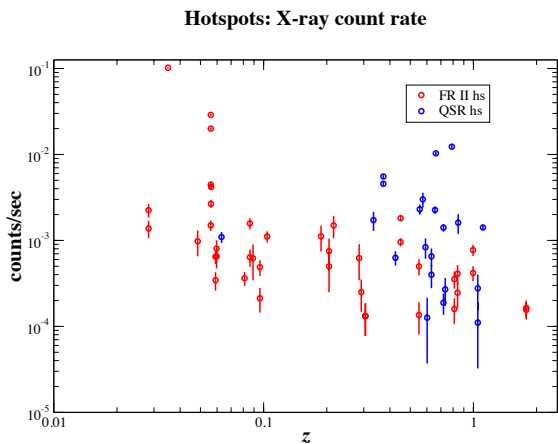


FIG. 4.— The X-ray count rate of hotspots in both RGs and QSRs with respect to the redshift.

in Figure 3 and Figure 4, respectively and the distribution of the X-ray count rate for the whole XJET sample in Figure 5. In detail, the distribution of the count rate for the whole XJET sample has an average count rate of  $5.5 \times 10^{-4} \pm 7.4 \times 10^{-6} \text{ s}^{-1}$  with a variance  $3.9 \times 10^{-6} \text{ s}^{-1}$ , corresponding to about 0.5 counts in 1 ksec similar to the peak of the X-ray count rate distribution, that is  $\sim 1$  count per 1 ks of exposure (see Figure 5). Note that the individual X-ray count rate distributions for the different components are reported in Figure 32 of Appendix A. The majority ( $\sim 3/4$ ) of the exposures are  $\sim 5$ -50 ksec in length with longer exposures up to 100-150 ksec for a handful of objects. The apparent lack of dependence of count rate on redshift is most likely caused by the limited sensitivity of most Chandra observations. For example, there are presumably large numbers of FRI jet knots at  $z > 0.1$  with count rates less than 10–4 counts/sec.

### 3. X-RAY DATA REDUCTION AND ANALYSIS

The *Chandra* data reduction has been performed following the standard reduction procedure described in the *Chandra* Interactive Analysis of Observations (CIAO)

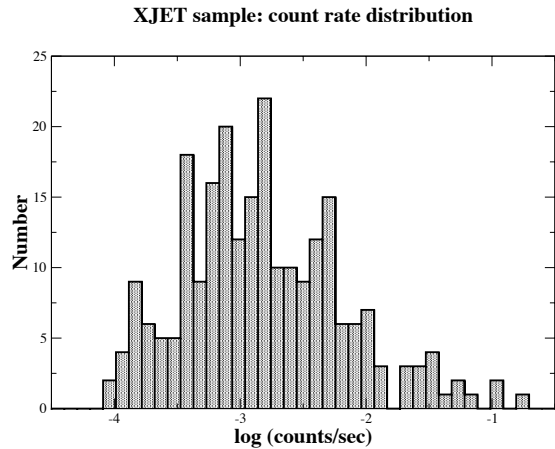


FIG. 5.— The count rate distribution for whole sample of XJET components detected in the X-rays.

threads<sup>6</sup>, using CIAO v4.2 and the Chandra Calibration Database (CALDB) version 4.2.2. All the data reduction and the data analysis procedures described in the following sections were adopted previously in our studies of 3C 305 (Massaro et al. 2009b) and 3C 17 (Massaro et al. 2009c), and for the ongoing *Chandra* 3C snapshot survey (Massaro et al. 2010b).

Specifically, level 2 event files were generated using the `acis_process_events` task, after removing the hot pixels with `acis_run_hotpix`. Events were filtered for grades 0, 2, 3, 4, 6 and we removed pixel randomization.

Light curves for every dataset were extracted and checked for high background intervals that have been excluded if the background count rate was found high over the whole back illuminated chip in the 7–10 keV energy range accordingly to the CIAO threads<sup>7</sup>.

Astrometric registration was achieved by changing the appropriate keywords (RA\_NOM, DEC\_NOM, TCRVL11, TCRVL12) in the fits header so as to align the nuclear X-ray position with that of the radio (i.e., the world coordinate system (WCS) of the X-ray image was shifted so it would be the same as the radio image).

#### 3.1. Fluxmaps

Following the standard reduction, we created fluxmaps in 3 defined bands (soft, medium, and hard, in the ranges 0.5–1, 1–2, and 2–7 keV, respectively) by dividing the data with monochromatic exposure maps (with nominal energies of soft=0.8 keV, medium=1.4 keV, and hard=4 keV). The exposure maps and the flux maps were regridded to a common pixel size which was usually 1/4 the size of a native ACIS pixel (native=0.492"). For sources of large angular extent we used 1/2 or no regridding. To obtain maps with brightness units of  $\text{ergs cm}^{-2} \text{ s}^{-1} \text{ pixel}^{-1}$ , we multiplied each event by the nominal energy of its respective band.

#### 3.2. Photometry

X-ray detected components were identified via visual inspection of the fluxmaps, referring to the detections

<sup>6</sup> <http://cxc.harvard.edu/ciao/guides/index.html>

<sup>7</sup> [http://cxc.harvard.edu/ciao/threads/filter\\_ltrcv/](http://cxc.harvard.edu/ciao/threads/filter_ltrcv/)

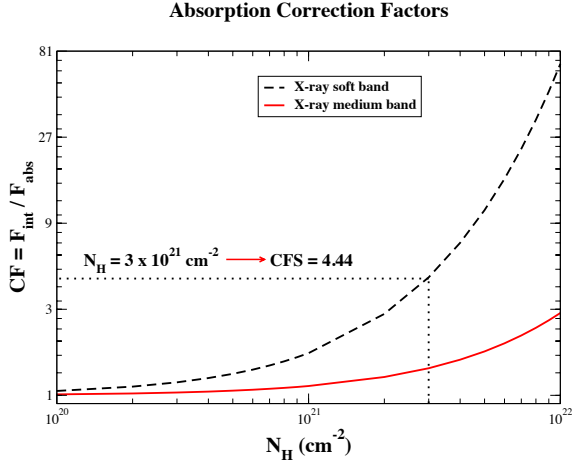


FIG. 6.— The correction factor,  $CF$ , estimated for the soft and the medium band, assuming an X-ray spectral index  $\alpha_X = 1$ , as a function of different values of the Galactic column density  $N_{\text{H}}$ . Our method used to derive the correction factor for the soft band is illustrated (see Section 3.3 for details).

published in the original references. To measure observed X-ray fluxes, we construct appropriate regions (usually circular) as well as two adjacent background regions of the same size (see e.g., Figure 1). The shape and the sizes of regions selected for our flux measurements are reported in Appendix A together with the radio and the X-ray fluxes for each component.

The net X-ray flux in each region for each band were measured using *funtools*<sup>8</sup>. After applying a small correction which is the ratio of the mean energy of the events within the ‘on’ aperture to the nominal energy applied earlier to all events, a  $1\sigma$  error is assigned based on the usual Poisson statistic  $\sqrt{\text{number} - \text{of} - \text{counts}}$  in the on and background regions.

### 3.3. Absorption corrections

To estimate the factors required to correct the observed X-ray fluxes for Galactic absorption we adopted the following method. We chose an arbitrary value of the intrinsic flux ( $F_{\text{int}}$ ) in each band (i.e., soft, medium, hard) and we computed the ratio between  $F_{\text{int}}$  and the absorbed flux  $F_{\text{abs}}$  for different values of  $N_{\text{H,Gal}}$  using the *WEBPIMMS* tool<sup>9</sup>. We considered  $N_{\text{H,Gal}}$  in the range between  $10^{20} \text{ cm}^{-2}$  and  $10^{22} \text{ cm}^{-2}$ , as for the sources in our sample (see Table 1, Table 2 and Table 3). We repeated this procedure for three representative values of the X-ray spectral index,  $\alpha_X = 0.5, 1.0$  and  $1.5$ .

In Figure 6, we show the plot of the correction factor,  $F_{\text{int}}/F_{\text{abs}}$  vs.  $N_{\text{H,Gal}}$  for the soft (0.5 – 1 keV) and the medium (1.0 – 2.0 keV) bands evaluated assuming  $\alpha_X = 1$ . For each source in Table 1, Table 2 and in Table 3, this ratio (again, for  $\alpha_X = 1$ ) appears in the column ‘CFS’ and ‘CFM’ for the X-ray soft and the medium band, respectively. For the range of  $N_{\text{H,Gal}}$  considered, we found  $< 7\%$  difference in the corrections assuming  $\alpha_X = 0.5$  and  $1.5$ . In addition, for our choice of the hard band (i.e., 2 – 7 keV), we found that the correction factor

for  $N_{\text{H,Gal}} \leq 10^{22} \text{ cm}^{-2}$  is always less than 1% different from unity for all three choices of the spectral index ( $\alpha_X = 0.5, 1.0$ , and  $1.5$ ). Thus the only significant corrections occur for the soft and the medium bands.

The X-ray fluxes reported (i.e., absorbed) in Appendix A are those measured for each component while those corrected for Galactic absorption were used in calculating the X-ray to radio flux ratios (see Section 4) and the X-ray hardness ratios (see section 5).

## 4. FLUX RATIOS

We developed one initial *parameter* to begin the investigation of the selected knots and hotspots. Using radio maps available in the public archives (e.g., NVAS<sup>10</sup>, NED<sup>11</sup>, and MERLIN<sup>12</sup>) or kindly provided by our colleagues, we measured the radio fluxes and computed  $\nu_R \times S_\nu(\nu_R)$  where the radio frequency of the maps used were,  $\nu_R = 1.4, 5$ , or  $8 \text{ GHz}$ . We then calculated the X-ray-to-radio flux ratio ( $\rho$ )

$$\rho = \frac{F_{0.5-7\text{keV}}}{\nu_R S(\nu_R)}, \quad (1)$$

where the X-ray fluxes (0.5 – 7 keV) are the totals from the three band fluxmaps corrected for Galactic absorption (see Section 3.3 for details). Observationally, this flux ratio is, to first order, independent of the redshift and it also is the same as the luminosity ratio, that hereinafter will be simply referred to as the *ratio*. All the main results derived from our analysis are reported in the Section 7.

We also note that for the X-ray to radio flux ratios, we utilized the integrated 0.5–7 keV X-ray fluxes (i.e.,  $F_{0.5-7\text{keV}}$ ) whereas in other works, the monochromatic ( $\nu S_\nu$ ) fluxes at both X-rays and radio are used (e.g. Cheung 2004; Kataoka & Stawarz 2005; Marshall et al. 2011). For the range of considered X-ray spectral indices,  $\alpha_X = 0.5 - 1.5$ , these monochromatic X-ray fluxes scale as:  $\nu S_\nu (1 \text{ keV}) = (0.26 - 0.48) \times F_{0.5-7\text{keV}}$ . Consequently the intrinsic dispersion in  $\alpha_X$  cannot be responsible for the observed dispersion of the ratios  $\rho$  (see Section 7).

Finally, we show the relation between our ratios  $\rho$  and the conventional radio-to-X-ray spectral index  $\alpha_{rx}$ . As is well known, a slope of -1 in a power-law radiation spectrum (i.e.  $S_\nu = k \nu^{-1}$ , with  $k$  the normalization) leads to equal energy per decade. However, since we have defined the ratio of X-ray flux to radio flux to be the measured flux in the 0.5 to 7 keV band divided by  $\nu_R S(\nu_R)$  (i.e. an approximation to a radio flux), a value of  $\rho = 1$  does not correspond to  $\alpha_{rx}=1$ . The actual relation is:

$$\rho = \nu_R^{(\alpha_{rx}-1)} \cdot \int_{\nu_1}^{\nu_2} \nu^{-\alpha_{rx}} d\nu, \quad (2)$$

where  $\nu_r$  is the observed radio frequency (Hz) and the integral is taken over the band from  $\nu_1 = 1.21 \times 10^{17}$  to  $\nu_2 = 1.69 \times 10^{18} \text{ Hz}$ . In Figure 7 we show the above relationship (i.e., Equation 2) for the three radio bands we have used in this work, namely: 1.5, 5, and 8 GHz.

<sup>8</sup> <http://www.cfa.harvard.edu/~john/funtools>

<sup>9</sup> <http://heasarc.nasa.gov/Tools/w3pimms.html>

<sup>10</sup> <http://www.aoc.nrao.edu/~vlbacald/>

<sup>11</sup> <http://nedwww.ipac.caltech.edu/>

<sup>12</sup> [http://www.jb.man.ac.uk/cgi-bin/merlin\\_retrieve.pl](http://www.jb.man.ac.uk/cgi-bin/merlin_retrieve.pl)

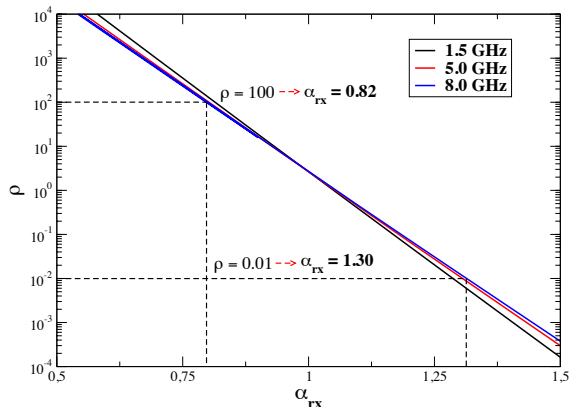


FIG. 7.— The relation between the luminosity ratios,  $\rho$  (see Equation 1) and the conventional radio-to-X-ray spectral index  $\alpha_{rx}$  estimated for three different radio frequencies (see Section 4 for more details).

Because most of our measured values of  $\rho$  fall between 0.01 and 100, it is fairly obvious that our total range can be described by a range of  $\alpha_{rx}$  from 0.7 to 1.3. Since we have not included radio knots which are not detected at X-rays, there will be larger values of  $\alpha_{rx}$  than 1.3. However, jet components with  $\alpha_{rx}$  significantly less than 0.7 have yet to be found.

Finally, we note that we did not apply any K-correction to our fluxes in order to estimate the luminosities in both the radio and the X-ray bands. Given the redshift distribution of our XJET sample, with only one exception, the highest value of  $z$  is  $\sim 2$ ; consequently, for values of the spectral slope  $\alpha$  between 0.5 and 1.5, the K-correction ranges between 0.58 and 1.73 and it does not affect our results, because it cannot be responsible for the large scatter of the observed luminosities and/or ratios (see Section 7). In particular, for the value  $\alpha = 1$ , used for the X-ray band to estimate the absorption correction factors (see Section 3.3), no K-correction is needed (e.g., Hogg 2000; Hogg et al. 2002).

## 5. X-RAY HARDNESS RATIOS

We also evaluated the X-ray hardness ratios (HRs) using the hard ( $H$ ), medium ( $M$ ), and soft ( $S$ ) X-ray fluxes corrected for the Galactic absorption, with the following relations:

$$HR_1 = \frac{H - M}{H + M}, HR_2 = \frac{H - S}{H + S}, HR_3 = \frac{M - S}{M + S}. \quad (3)$$

We note that because HRs are defined using X-ray fluxes, there is a relationship between the X-ray spectral index ( $\alpha_X$ ) and HRs for any given selection of energy bands (e.g., Figure 8). In this way, the X-ray HRs serve as a reasonable surrogate for the  $\alpha_X$  of these extended components because the short exposures of the available X-ray observations combined with their low intrinsic flux (i.e.,  $\sim 10^{-15}$  erg s $^{-1}$  cm $^{-2}$ ) do not allow us to estimate values of  $\alpha_X$  with the usual spectral tools (e.g. Sherpa, XSPEC etc.) for the whole sample. However, as the current HR values do not provide robust constraints on  $\alpha_X$ , this conclusion should be revisited over a wide sample of source when deep X-ray observations will be available

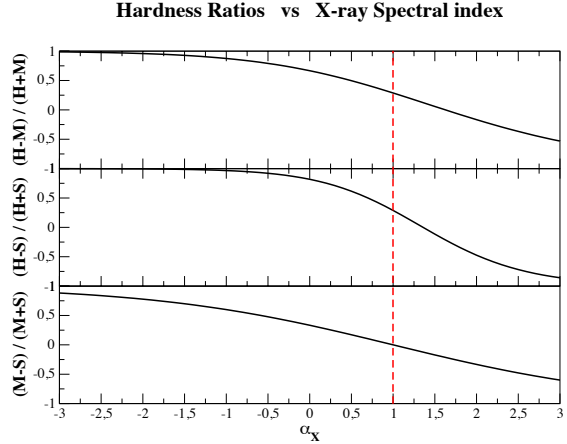


FIG. 8.— The relation between the hardness ratios,  $HR_1$  (upper panel),  $HR_2$  (middle panel) and  $HR_3$  (lower panel), defined by Equation (3) and the X-ray spectral slope  $\alpha_X$ .

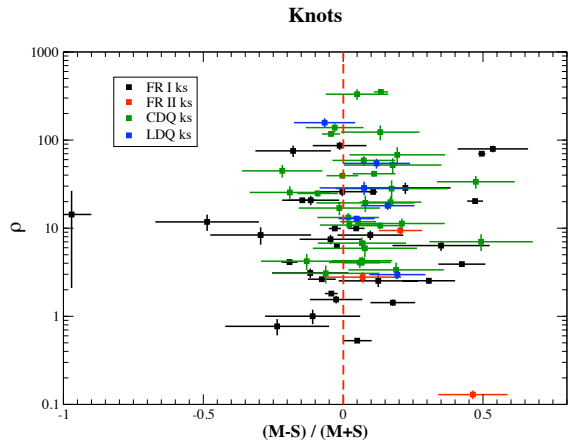


FIG. 9.— The ratios *vs* the hardness ratios  $HR_3$  (see Equation 3) for knots. We only considered those components for which the error on the  $HR_3$  is lower than 0.2. The red dashed line corresponds to  $\alpha_X = 1$  (see Figure 8 for more details).

that will further limit the error on the HRs, also involving the Bayesian analysis (Park et al. 2006). In Figure 9 and Figure 10 we report the ratios with respect to the hardness ratios  $HR_3$  only for those sources for which the error on  $HR_3$  is lower than 0.2, no significant trend is evident.

We compare all the values of  $\rho$  and HRs dividing the knots and the hotspots of our sources in 6 categories as defined in Section 2. We did not find any significant difference in the distributions of the HRs between RGs and QSRs.

Finally, we note that given the small number of BL Lacs in our sample, and the limited number of their components (i.e., only 7 out of 236), we did not consider the comparison between this class of object and the RGs or the QSRs not only regarding the HRs but also with respect to the other parameters.

## 6. THE KS TEST AND THE MONTE CARLO SIMULATIONS



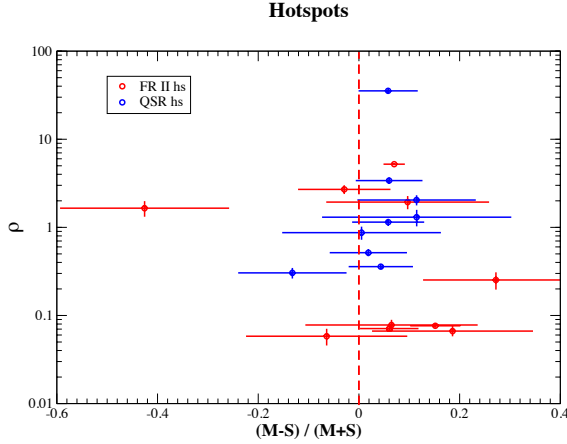


FIG. 10.— The ratios  $\rho$  vs the hardness ratios  $HR_3$  (see Equation 3) for hotspots. We only considered those components for which the error on the  $HR_3$  is lower than 0.2. The red dashed line corresponds to  $\alpha_X = 1$  (see Figure 8 for more details).

To search for possible differences or similarities between knots and hotspots both in RGs and QSRs, we compared the distributions of the observed parameters such as the luminosities (both  $L_R$  and  $L_X$ ), their ratios ( $\rho$ ), and their HRs as defined in Equation 3.

To perform our analysis, we adopted a Kolmogorov-Smirnov (KS) test, measuring the distance  $D_{KS}$  between the normalized cumulative distributions of parameters for two different samples of components and estimating the associated probability to test our hypothesis. However, because our selected sample is not statistically complete, our analysis could be affected by some biases. Consequently, it is possible to measure a large value of  $D_{KS}$  between two selected cumulative distributions, suggesting that they are different, simply because of the lack of sources in a particular bin of our histograms. This could strongly affect our analysis and our results. To check the significance of results provided by the KS test, we developed a Monte Carlo method to take into account this effect and to estimate its relevance.

We illustrate this method for the simple case to test if the distributions of radio luminosities  $L_R$  in RGs and QSRs are similar or different (see Figure 11).

First, we performed the KS test and we measured the  $D_{KS}$  in the  $L_R$  normalized cumulative distributions. Second, we randomly simulate the two distributions of  $L_R$  for both cases of hotspots in RGs and QSRs, with the same number of components (i.e., 41 hs2 and 21 hsq). We adopted two different shapes for the simulated distributions, the log-uniform and the log-normal. The former having simply the same maximum and minimum value of the observed distribution while the latter with the same variance, the same median of the observed distribution and spanning the same range of luminosities (see Table 4). Then, we measured the  $D_{KS,simul}$  variable between the two simulated distributions.

We repeated the simulation 8000 times and we built the distribution of the  $D_{KS,simul}$  distance (see Figure 12, for the case of the log-uniform distribution). Finally, we estimated the probability to obtain, randomly, the observed  $D_{KS}$ , and this provides us the level of confidence

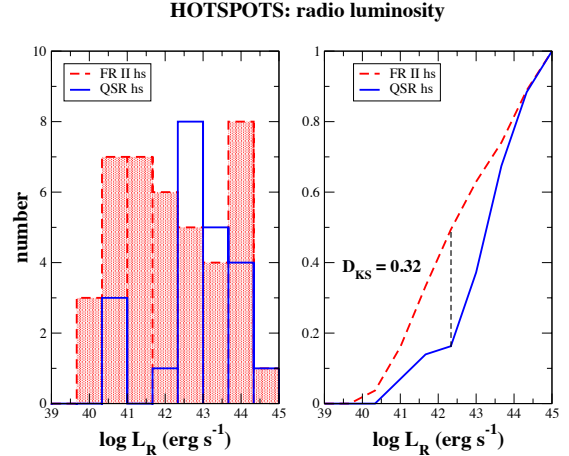


FIG. 11.— Left panel) The  $L_R$  distributions for the hotspots in the FR II RGs (dashed red lines) and LDQs (blue solid line). Right panel) The normalized cumulative distributions of the radio luminosities for the hotspots in FR IIs and in LDQs.

of our KS test (see Figure 12, lower panel).

The levels of confidence (i.e., probabilities) derived from Monte Carlo simulations performed to generate the two hotspot distributions of  $L_R$ , run adopting both the log-uniform and log-normal function are reported in Table 5 and Table 6 for the two different cases. Adopting the log-uniform function for the simulated distributions in the case of the ratio comparison, because these depend only by the maximum and the minimum value of  $\rho$ , that is roughly the same for all components does not provide a meaningful and significative check of the KS test. Thus, we do not report the  $P(D_{KS})^u$  for the ratio comparison. This problem does not occur in the case of the log-normal distribution because it is described by more parameters than the log-uniform.

In both Tables 5 and 6, Col. (1) and Col. (2) show the two components compared. Col. (3) reports the observed parameter and Col. (4) the KS variable  $D_{KS}$  measured of the observed distributions. Col.(5) show the probability of the Monte Carlo simulations assuming a log-uniform distribution (i.e.,  $P(D_{KS})^u$ ) while that of a log-normal is reported in Col. (6) (i.e.,  $P(D_{KS})^g$ ).

Finally, we note that, unfortunately, due to the short exposures of X-ray observations for the majority of the selected sources, a statistical analysis of their HRs cannot be performed. Consequently, no firm conclusions can be obtained from our investigation on the average spectral behavior of different source classes and no results are reported in the following sections. The errors on the single source HRs are too large to allow a statistically significant comparison between their distributions.

## 7. RESULTS

The average properties (i.e., max, min values, median and variance of  $L_R$ ,  $L_X$  and  $\rho$ ) for all the class components are reported in Table 4, while the level of confidences derived from our Monte Carlo simulations are shown in Table 5 and 6 as described in Section 6. Here, we discuss the main observational results derived from our investigation.

When comparing the radio and the X-ray luminosities possible biases could arise from the the different red-

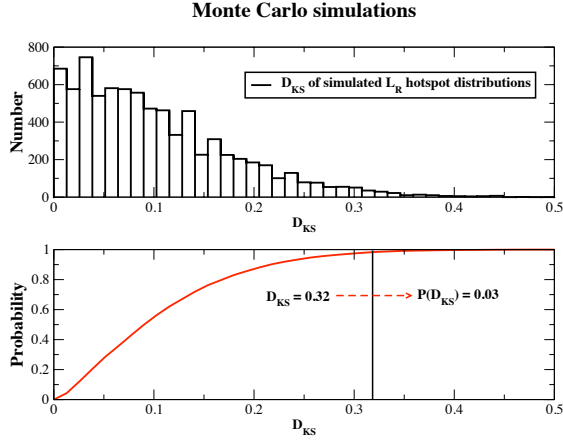


FIG. 12.— Upper panel) The  $D_{KS}$  between the two cumulative normalized  $L_R$  distributions of hotspots in FR IIs and LDQs simulated via the Monte Carlo method as described in Section 6. Lower panel) The probability to obtain randomly the observed  $D_{KS}$  assuming a log-uniform shape for the simulated  $L_R$  hotspots distributions (see Section 6 for more details).

shift distributions of RGs and QSRs. For example, QSRs could appear more luminous than FRIs simply because they lie at higher redshift, where the low luminosity RGs would be too faint for detection. However, this will not affect the comparison of the ratios. The ratios could be affected by biases of the incompleteness of our source sample, but this problem have been addressed by using the MonteCarlo simulations (see Section 6). Finally, we note that to make the redshift distribution more uniform future Chandra observations of both QSRs and RGs have been proposed.

### 7.1. Hotspots

The components that can be morphologically classified as hotspots are only present in FR IIs (hs2) and in QSRs (hsq). We compared the distributions of their radio and X-ray luminosity (i.e.,  $L_R$ ,  $L_X$ ) and also of their ratios (i.e.,  $\rho$ ) (see Figure 17 in Appendix A).

We found that hotspots in FR IIs and in LDQs do not show significant differences in the distributions of  $L_R$  and  $L_X$ , and they appear to have also similar  $\rho$  distribution. We also note that the hs2 are the only components for which the average value of  $\rho$  is lower than one (see Table 4). In Figure 13 we show the ratios *vs* both  $L_R$  and  $L_X$  for the hotspots. There is a marginal trend between  $\rho$  and  $L_R$  where hotspots in both RGs and QSRs, with high values of  $\rho$  have typically low values of  $L_R$ , in agreement with the results found in Hardcastle et al. (2004). However, because the two variables  $\rho$  and  $L_R$  are not independent the estimate of their correlation coefficient will not be statistically meaningful. In Figure 14 we report the  $\rho$  values as a function of the projected distance, where no clear trend has been found.

### 7.2. Knots

First, we compared knots between RGs (i.e., FR Is vs FR IIs) and between QSR classes (CDQs vs LDQs), then we considered also the comparison between RGs and QSRs.

1.) *k1 vs k2*. Knots in FR Is are less powerful in  $L_R$

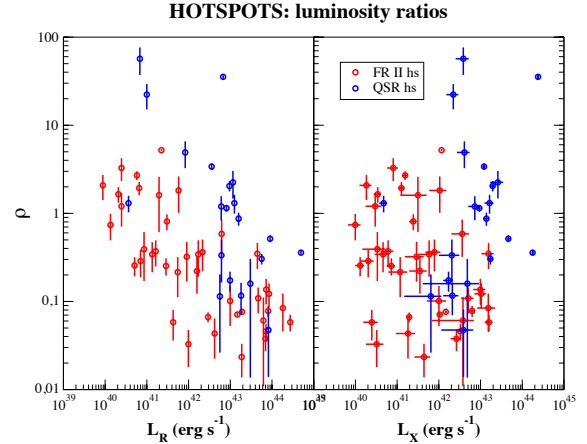


FIG. 13.— The behavior of ratios measured for the hotspots in FR IIs (hs2) and in QSRs (hsq) with respect to the radio luminosity  $L_R$  (left panel) and the X-ray luminosity  $L_X$  (right panel).

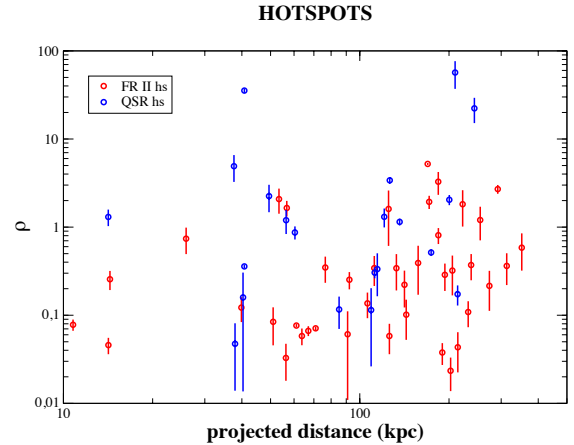


FIG. 14.— The ratios measured for the hotspots in FR IIs (hs2) and in QSRs (hsq) as function of the projected distance from the core in kpc.

than knots in FR IIs (see Figure 18 in Appendix A). There is no significant difference in  $L_X$  and  $\rho$  between k1 and k2 components even if the probability given from our Monte Carlo method is not very high, as reported in Table 5. However, the FR II  $L_R$  distribution is not well sampled as is the case for FR Is, that has about 3 times the number of components with respect to the former, requiring a deeper investigation to confirm these results.

2.) *kqc vs kql*. The situation of QSR knots is very different with respect to that of RGs (see Figure 19 in Appendix A). We did not find any difference between knots in CDQs and LDQs. All their distributions of  $L_R$ ,  $L_X$  and  $\rho$  are identical, within the level of confidence provided by the Monte Carlo simulations (see Table 5).

3.) *k1 vs kq*. Comparing the FR I with the CDQ knots we found that: k1 components are systematically different in  $L_R$  and  $L_X$  distributions than kqc components with a high level of confidence (see Table 5). CDQ knots appear to be systematically brighter than FR I knots in both the radio and the X-ray band. On the other hand,

TABLE 4  
 THE AVERAGE PROPERTIES OF THE EXTENDED COMPONENTS.

Class	Num.	$\log L_{R,\min}$ erg s <sup>-1</sup>	$\log L_{R,\max}$ erg s <sup>-1</sup>	$\langle \log L_R \rangle$ erg s <sup>-1</sup>	$\log L_{X,\min}$ erg s <sup>-1</sup>	$\log L_{X,\max}$ erg s <sup>-1</sup>	$\langle \log L_X \rangle$ erg s <sup>-1</sup>	$\langle \log \rho \rangle$
FR I ks (k1)	58	36.9	41.7	38.82(1.05)	37.0	42.1	40.04(0.24)	+1.13(0.26)
FR II ks (k2)	22	38.9	43.3	40.05(1.80)	39.1	42.5	41.18(0.81)	+0.58(0.79)
CDQ ks (kqc)	68	39.3	44.3	41.11(0.97)	40.4	45.2	43.20(0.75)	+1.73(0.48)
LDQ ks (kql)	19	40.3	44.4	42.67(1.28)	41.4	45.2	43.64(0.65)	+1.15(0.33)
FR II hs (hs2)	41	39.9	44.4	42.17(1.69)	40.0	43.2	41.99(0.19)	-0.11(0.79)
QSR hs (hsq)	21	40.5	43.9	42.86(0.99)	40.6	44.3	43.70(0.53)	+0.24(0.61)

Note: for each average parameter we also report the variance of its distribution in parenthesis.

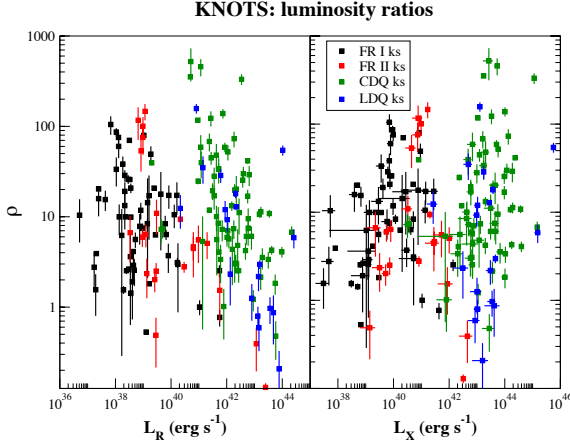


FIG. 15.— The behavior of ratios measured for the knots in RGs and in QSRs with respect to the radio luminosity  $L_R$  (left panel) and the X-ray luminosity  $L_X$  (right panel).

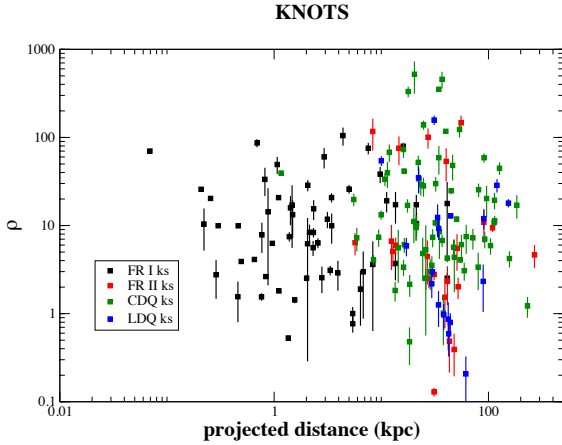


FIG. 16.— The ratios measured for the hotspots in RGs and in QSRs as function of the projected distance from the core in kpc.

their ratio distributions are similar (see Figure 20, Figure 21 in Appendix A). The same behavior has been found comparing knots in FR Is and in LDQs, where they appear to be significantly different and brighter in both the  $L_R$  and  $L_X$  distributions but having similar ratios.

4.)  $k2$  vs  $kq$ . The comparison between knots in FR IIs and QSR is the same for both classes (i.e., CDQ and LDQ) (see Figure 23, Figure 22 in Appendix A). The

TABLE 5  
 THE KS TEST AND THE RESULTS OF THE MONTE CARLO METHOD (SEE SECTION 6) PERFORMED TO COMPARE THE RG AND QSR PARAMETER DISTRIBUTIONS OF KNOTS AND HOTSPOTS, SEPARATELY.

Type 1	Type 2	Param.	$D_{KS}$	$P(D_{KS})^u$	$P(D_{KS})^g$
hs2	hsq	$\log L_R$	0.32	0.03	0.35
hs2	hsq	$\log L_X$	0.57	0.00	0.33
hs2	hsq	$\log \rho$	0.17	—	0.55
k1	k2	$\log L_R$	0.25	0.04	0.05
k1	kqc	$\log L_R$	0.82	0.00	0.00
k1	kql	$\log L_R$	0.83	0.00	0.00
k2	kqc	$\log L_R$	0.60	0.00	0.00
k2	kql	$\log L_R$	0.70	0.00	0.00
kqc	kql	$\log L_R$	0.22	0.07	0.68
k1	k2	$\log L_X$	0.14	0.24	0.68
k1	kqc	$\log L_X$	0.88	0.00	0.00
k1	kql	$\log L_X$	0.91	0.00	0.00
k2	kqc	$\log L_X$	0.86	0.00	0.00
k2	kql	$\log L_X$	0.95	0.00	0.00
kqc	kql	$\log L_X$	0.03	0.82	0.94
k1	k2	$\log \rho$	0.08	—	0.73
k1	kqc	$\log \rho$	0.04	—	0.88
k1	kql	$\log \rho$	0.11	—	0.71
k2	kqc	$\log \rho$	0.11	—	0.66
k2	kql	$\log \rho$	0.05	—	0.75
kqc	kql	$\log \rho$	0.14	—	0.43

$k2$  components show similar  $\rho$  distributions, while they appear to be significantly fainter than  $kq$  components in both  $L_X$  and  $L_R$  distributions even if with a small difference in the probability provided by the Monte Carlo method (see Table 5). In Figure 15 we show the ratios  $\rho$  vs both the  $L_R$  and  $L_X$  luminosities for the knots, while in Figure 16 we report the  $\rho$  values as a function of the projected distance, in both cases no clear trend or correlation has been found between the observed parameters.

Finally, we note the presence of a few red filled squares with  $\rho < 1$ , shown in both Figure 15 and Figure 16, these  $k2$  components belong to three different FR II RGs, as the case of 3C 353, that with  $z = 0.0304$  is also the second closest FR II RG in our sample (the closest is PKS2153-69 at  $z = 0.0283$ ).

These  $k2$  components have been detected because the exposures of these source observations are the longest among the whole FR II RGs, a crucial test to verify if other  $k2$  knots show similar values of ratios could be provided by deeper observations of radio sources in the same class. These ‘low ratio’ knots in these FR II RGs represent a clear example of a bias that could appear in the KS test. In fact, they can make the  $k2$  ratio distribu-

tion different from the real one, because the number of components in FR IIs is lower with respect to the other classes (i.e., 20), resulting in a large value of the  $D_{KS}$  variable (see Table 5).

However, our Monte Carlo method developed to take into account this problem, shows that the differences in  $\rho$  between k2 and other knots are marginal. A better investigation of the k2 ratio distribution might be possible in the future if/when deeper *Chandra* observations will be performed.

### 7.3. Hotspots vs Knots

We compared hotspots and knots in RGs and QSRs and between them.

1.) *k1 vs hs2*. We found that hs2 components are different in  $L_R$  and  $\rho$  with respect to k1 ones, being less bright at radio frequencies, while their  $L_X$  distribution is roughly similar (see Figure 24).

2.) *k2 vs hs2*. No significant differences have been found in both the  $L_X$  distributions comparing hotspots and knots of FR II RGs (see Figure 25), while their  $L_R$  and  $\rho$  distributions appear different as for k1 components.

3.) *kq vs hs2*. Comparing hotspots in RGs (hs2) with knots in QSR (i.e., both kqc and kql), we found no significant differences in their  $L_R$  distribution while they appear to be extremely different in the  $L_X$  distributions, where kq components are brighter than hs2 ones. Consequently also their  $\rho$  distributions are significantly different (see Figure 26 and Figure 27).

4.) *k1 vs hsq*. Knots in FR Is appear very different in  $L_R$ ,  $L_X$  and  $\rho$  distributions with respect to hotspots in QSRs (see Figure 28). FRI knots are systematically fainter than hsq components at radio and X-ray frequencies.

5.) *k2 vs hsq*. In the case of FR II knots (i.e., k2), the situation is similar to that of k1 components in comparison with hsq. Even if k2 are different in  $L_R$  and in  $L_X$  with respect to hsq, their  $\rho$  distribution appear to be similar (see Figure 29) within our level of confidence (see Table 6). However, we note that this comparison regards the two classes with the smallest number of components, that could be more affected by statistical biases. Thus to confirm this result an investigation on a larger sample than the one considered is necessary.

6.) *kqc vs hsq*. The behavior of hotspots vs knots in QSRs appear to be different from that in RGs. We did not find any significant difference between hsq and kqc components in their  $L_R$  and  $L_X$  distributions, there is only a significant difference in their  $\rho$  distribution (see Figure 30). In addition, kqc components have  $\rho$  values systematically higher than 1, while the average  $\rho$  of hsq is closer to zero (see Table 4).

7.) *kql vs hsq*. Also the  $L_R$  and  $L_X$  distributions of hsq and kql components are similar within the probabilities as indicated by our statistical analysis, while a marginal difference has been found in the  $\rho$  distribution (see Figure 31), less significant than that found between kqc and hsq components, because of the smaller number of knots considered.

Finally, we note that the most statistically significant differences we found regard the comparison between all the parameter distributions of knots in RGs and hotspots in QSRs. Both the kqc and kql components are significantly different in all the  $L_R$ ,  $L_X$ ,  $\rho$  distributions, with

TABLE 6  
THE KS TEST AND THE RESULTS OF THE MONTE CARLO METHOD (SEE SECTION 6) PERFORMED TO COMPARE THE PARAMETER DISTRIBUTIONS BETWEEN KNOTS AND HOTSPOTS.

Type 1	Type 2	Param.	$D_{KS}$	$P(D_{KS})^u$	$P(D_{KS})^g$
k1	hs2	$\log L_R$	0.78	0.00	0.00
k2	hs2	$\log L_R$	0.55	0.00	0.00
k1	hs2	$\log L_X$	0.60	0.00	0.06
k2	hs2	$\log L_X$	0.21	0.10	0.64
k1	hs2	$\log \rho$	0.74	—	0.00
k2	hs2	$\log \rho$	0.66	—	0.00
kqc	hs2	$\log L_R$	0.16	0.16	0.54
kql	hs2	$\log L_R$	0.20	0.14	0.51
kqc	hs2	$\log L_X$	0.59	0.00	0.06
kql	hs2	$\log L_X$	0.68	0.00	0.00
kqc	hs2	$\log \rho$	0.77	—	0.00
kql	hs2	$\log \rho$	0.62	—	0.00
k1	hsq	$\log L_R$	0.84	0.00	0.00
k2	hsq	$\log L_R$	0.73	0.00	0.00
k1	hsq	$\log L_X$	0.83	0.00	0.00
k2	hsq	$\log L_X$	0.64	0.00	0.00
k1	hsq	$\log \rho$	0.42	—	0.04
k2	hsq	$\log \rho$	0.38	—	0.36
kqc	hsq	$\log L_R$	0.38	0.00	0.10
kql	hsq	$\log L_R$	0.19	0.23	0.35
kqc	hsq	$\log L_X$	0.12	0.31	0.51
kql	hsq	$\log L_X$	0.17	0.30	0.41
kqc	hsq	$\log \rho$	0.50	—	0.00
kql	hsq	$\log \rho$	0.33	—	0.49

respect to the hs2 ones.

## 8. DISCUSSION AND SUMMARY

The chief reason we investigated the ratios of X-ray to radio fluxes was the expectation that there would be substantial differences between components commonly thought to be synchrotron X-ray sources (e.g., FRI knots) and those thought to come from inverse Compton scattering off the Cosmic Microwave Background (IC/CMB) (Bergamini et al. 1967; Tavecchio et al. 2000; Celotti et al. 2001) dominated emission (e.g., QSR knots). In this section we compare the observed results with various “expectations” associated with the two emission processes.

In a sense, the most surprising result is that the  $\rho$  distributions for FRI knots is essentially indistinguishable from that for QSR knots. If the X-rays from both classes of objects are dominated by synchrotron emission there would be no reason for surprise: the observed spread in  $\rho$  would reflect the spread in the ratio of amplitudes of the electron spectra between the energies responsible for the X-rays and those responsible for the radio. However, if the X-ray emission from QSR knots is actually IC/CMB, we must deduce that the factors contributing to  $\langle \rho \rangle$  and the width of the  $\rho$  distribution conspire to produce the same results for FRI and QSR knots. In the synchrotron case these factors are those described above.

In the IC/CMB model,  $\rho$  is mainly dependent on three factors: the ratio of amplitudes of the electron energy spectra around  $\gamma \approx 10^2$  emitting in the X-rays to those producing the observed radio emission at GHz frequencies (i.e.,  $\gamma \approx 10^4$ ), the ratio of the bulk Lorentz factor

$\Gamma$  over the magnetic field  $B$ , as  $(\Gamma/B)^2$ , and an additional broadening of the  $\rho$  distribution arising from the dispersion in the distribution of the angle between the velocity vector of the jet knot and the line-of-sight in different sources (Harris et al. 2010). Our expectation was that these completely different factors would produce substantially different  $\rho$  distributions, however, we found no significant differences between the QSRs and FRIs in this respect.

Another difference between the two emission processes is the additional bulk Lorentz factor in the IC/CMB model stemming from the fact that head-on IC scattering is more probable than over-taking scattering (i.e., “extra-beaming factor”) (Dermer 1995; Harris & Krawczynski 2002; Massaro et al. 2009c). Statistically, this feature should manifest most prominently when comparing sources with small angles between our line-of-sight and the jet to those with larger angles. In our sample, we have both LDQs and CDQs, and it is commonly believed that the determining factor for this division is that CDQs have jets closer to the line-of-sight. Thus we might expect larger  $\rho$  values for CDQs than LDQs. This prediction was not found in our current data. A possible interpretation of the lack of differences between knots in CDQs and in LDQs is that the sampling of Chandra observations (and subsequent x-ray jet detections compiled in XJET) have tended toward sampling of the most ‘aligned’ sources (i.e., the most core-dominated) in general. Future observations of LDQs characterized with systematically lower radio core-dominance values than currently probed may make any differences apparent. Alternative explanations include that most jets of CDQs bend significantly between the inner (pc-scale) and the outer (kpc-scale).

One of the few real differences in  $\rho$  distributions occurs when one compares FR II hotspots to knots (both in RGs and QSRs). Most FR II hotspots have  $\rho < 1$  whereas most knots have  $\rho > 1$ . This effect finds a reasonable cause in our current understanding of X-ray emission from hotspots (Hardcastle et al. 2004). The more powerful radio hotspots are consistent with a synchrotron self-Compton (SSC) model for the dominant X-ray emission process. As shown in Figure 13, the FR II hotspots with  $\rho > 1$  all have  $L_r < 10^{42}$  erg s $^{-1}$ , and these lower luminosity hotspots are those for which SSC is thought not to be the dominant X-ray emission process (Hardcastle et al. 2004) but rather, an additional emission mechanism (synchrotron or additional IC) may be responsible for the observed X-rays.

More details about the interpretations of the above results and the comparison between the theoretical expectations and the observational evidences will be dis-

cussed in forthcoming papers (Harris et al. 2011) where these results will be also compared with those on RGs found by Kataoka & Stawarz (2005). Finally, a possible statistical test for the IC/CMB process in QSRs will be described in (Massaro et al. 2011b).

We thank the anonymous referee for useful comments that led to improvements in the paper. We are extremely grateful to our friends and colleagues: T. Aldcroft, M. Birkinshaw, A. Bliss, K. Blundell, D. Evans, J. Gelbord, G. Giovannini, M. Hardcastle, P. Kharb, R. Kraft, S. Jorstad, R. Laing, J. Leahy, M. Lister, C. Ly, A. Marscher, H. Marshall, B. Miller, R. Morganti, D. Schwartz, A. Siemiginowska, and D. Worrall, for providing radio maps; their contribution has been crucial to carry on our investigation. F. Massaro thanks A. Cavaliere, G. Brunetti, G. Giovannini and G. Migliori for fruitful discussions, and R. D’Abrusco for his suggestions on compiling the tables.

This research has made use of SAOImage DS9, developed by the Smithsonian Astrophysical Observatory (SAO) and the NASA/IPAC Extragalactic Database (NED) which is operated by the Jet Propulsion Laboratory, California Institute of Technology, under contract with the National Aeronautics and Space Administration. TOPCAT<sup>13</sup> (Taylor 2005) was used extensively in this work for the preparation and manipulation of the tabular data. Several radio maps were downloaded from the NVAS (NRAO VLA Archive Survey) and from the MERLIN archive. The National Radio Astronomy Observatory is operated by Associated Universities, Inc., under contract with the National Science Foundation. MERLIN is a National Facility operated by the University of Manchester at Jodrell Bank Observatory on behalf of STFC. The Australia Telescope is funded by the Commonwealth of Australia for operation as a National Facility managed by CSIRO. This research has made use of data obtained through the High Energy Astrophysics Science Archive Research Center Online Service, provided by the NASA/Goddard Space Flight Center.

F. Massaro acknowledges the Fondazione Angelo Della Riccia for the grant awarded him to support his research at SAO during 2011. The XJET website is partially supported by NASA grant AR6-7013X and NASA contract NAS8-39073. The work at SAO was supported by NASA-GRANTS GO8-9114A and NNX10AD50G. F. Massaro acknowledges the Foundation BLANCEFLOR Boncompagni-Ludovisi, n’ee Bildt for the grants awarded him in 2009 and in 2010 to support his research at SAO.

**Facilities:** CXO (ACIS), VLA, MERLIN, ATCA

## REFERENCES

- Aldcroft, T.L., Siemiginowska, A., Elvis, M., Mathur, S., Nicastro, F., & Murray, S.S. 2003 ApJ, 597 751  
 Barthel, P. D. 1989 ApJ, 336, 606  
 Bergamini, R., Londrillo, P., Setti, G. 1967, NCimB, 52, 495  
 Birkinshaw, M., Worrall, D.M., & Hardcastle, M.J. 2002 MNRAS, 335, 142  
 Bondi, M., Brunetti, G., Comastri, A., & Setti, G. 2004, MNRAS, 354, L43  
 Bridle, A. H. 1986, Can. J. Phys., 64, 353  
 Brunetti, G., Bondi, M., Comastri, A., & Setti, G. 2002, A&A, 381, 795  
 Celotti, A., Ghisellini, G., & Chiaberge, M. 2001, MNRAS, 321, L1  
 Chartas, G., Gupta, V., Garmire, G., Jones, C., Falco, E.E., Shapiro, I.L., & Tavecchio, F. 2002, ApJ, 565, 96  
 Cheung, C.C. 2004, ApJL, 600, L23  
 Cheung, C.C., Stawarz, L., & Siemiginowska, A. 2006 ApJ, 650, 679  
 Chiaberge, M., Gilli, R., Macchetto, F.D., Sparks, W.B., & Capetti, A. 2003 ApJ, 582, 645

<sup>13</sup> <http://www.star.bris.ac.uk/~mbt/topcat/>

- Comastri, A., Brunetti, G., Dallacasa, D., Bondi, M., Pedani, M., & Setti, G. 2003, *MNRAS*, 340, L52
- Crawford, C.S., & Fabian, A.C. 2003, *MNRAS*, 339, 1163
- Dermer, C. D. 1995 *ApJ*, 446, L63
- Donahue, M., Daly, R.A., & Horner, D.J. 2003, *ApJ*, 584, 643
- Dunkley, J., et al. 2009 *ApJS*, 180, 306
- Evans, D.A., Hardcastle, M.J., Croston, J.H., Worrall, D.M., & Birkinshaw, M. 2005, *MNRAS*, 359, 363
- Fabian, A.C., Celotti, A., & Johnstone, R.M. 2003a *MNRAS*, 338, L7
- Fabian, A.C., Sanders, J.S., Crawford, C.S., & Etori, S. 2003b *MNRAS*, 341, 729
- Fanaroff, B. L. & Riley J. M. 1974, *MNRAS*, 167, P31
- Finoguenov, A., Ruszkowski, M., Jones, C., Brggen, M., Vikhlinin, A., Mandel, E.
- Gelbord, J.M. et al. 2005, *ApJ*, 632, L75
- Hardcastle, M.J., Birkinshaw, M., & Worrall, D.M. 2001 *MNRAS*, 323, L17
- Hardcastle, M.J., Birkinshaw, M., & Worrall, D.M. 2001 *MNRAS*, 326, 1499
- Hardcastle, M.J., Worrall, D.M., Birkinshaw, M., Laing, R.A., & Bridle, A.H. 2002a *MNRAS*, 334, 182
- Hardcastle, M.J., Birkinshaw, M., Cameron, R.A., Harris, D.E., Looney, L.W., & Worrall, D.M. 2002b, *ApJ*, 581, 948
- Hardcastle, M. J., Harris, D. E., Worrall, D. M., Birkinshaw, M. 2004, *ApJ*, 612, 729
- Hardcastle, M.J., Worrall, D.M., Birkinshaw, M, Laing, R.A., & Bridle, A.H. 2005a *MNRAS*, 358, 843
- Hardcastle, M.J., Sakelliou, I., & Worrall, D.M. 2005b, *MNRAS*, 359, 1007
- Hardcastle, M.J., Croston, J.H., & Kraft, R.P. 2007 *ApJ*, 669, 893
- Harris, D.E., et al. 2000 *ApJ*, 530, L81
- Harris, D. E., Krawczynski, H. 2002, *ApJ*, 565, 244
- Harris, D.E., Krawczynski, H., & Taylor, G.B. 2002a *ApJ*, 578, 740
- Harris, D.E., Mossman, A.E., & Walker, R.C. 2004a *ApJ*, 615, 161
- Harris, D. E., Krawczynski, H. 2006, *ARA&A*, 44, 463
- Harris, D. E., Massaro, F., Cheung, C. C. 2010, *AIPC*, 1248, 355
- Harris, D. E., Massaro, F., Cheung, C. C. 2011 in prep.
- Hine, R. G. & Scheuer, P. A. G. 1980 *MNRAS*, 193, 285
- Hodges-Kluck, E.J., Reynolds, C.S., Miller, M.C., Cheung, C.C. 2010 *ApJL*, 717, L37
- Hogan, B.S., Lister, M.L., Kharb, P., Marshall, H.L., Cooper, N.J. 2011 *ApJ*, 730, 92
- Hogg, D. W. [arXiv:astro-ph/9905116v4](https://arxiv.org/abs/astro-ph/9905116v4)
- Hogg, D. W., Baldry, I. K., Blanton M. R. & Eisenstein D. J. [arXiv:astro-ph/0210394v1](https://arxiv.org/abs/astro-ph/0210394v1)
- Hough, D. H. & Readhead, A. C. S. 1989, *AJ*, 98, 1208
- Kendall, M., & Stuart, A., 1979, "The Advanced Theory of Statistics," Mac Millan, New York
- Kalberla, P.M.W., Burton, W. B., Hartmann, D., et al. 2005, *A&A*, 440, 775
- Kataoka, J., Edwards, P., Georganopoulos, M., Takahara, F., & Wagner, S. 2003a, *A&A*, 399, 91
- Kataoka, J., Leahy, J.P., Edwards, P.G., Kino, M., Takahara, F., Serino, Y., Kawai, N., & Martel, A.R. 2003b *A&A*, 410, 833
- Kataoka, J. & Stawarz, L. 2005, *ApJ*, 622, 797
- Kataoka, J. et al. 2008, *ApJ*, 685, 839
- Kraft, R.P. et al. 2000 *ApJ*, 531, L9
- Kraft, R.P., Hardcastle, M.J., Worrall, D.M., & Murray, S.S. 2005, *ApJ*, 622, 149
- Kraft, R.P., Birkinshaw, M., Hardcastle, M.J., Evans, D.A., Croston, J.H., Worrall, D.M., & Murray, S.S. 2007 *ApJ*, 659, 1008
- Jester, S., Harris, D. E., Marshall, H. L., Meisenheimer, K. 2006, *ApJ*, 648, 900
- Jorstad, S., & Marscher, A. 2004 *ApJ*, 614, 615
- Jorstad, S.G. & Marscher, A.P. 2006, *Astr. Nach.*, 327, 227
- Landt, H., Padovani, P., Perlman, E. S., Giommi, P. 2004 *MNRAS*, 351, 83
- Landt, H., Perlman, E. S., Padovani, P. 2006 *ApJ*, 637, 183
- Leahy, J. P. et al. 1997, *MNRAS*, 291, 20
- Ly, C., De Young, D., & Bechtold, J. 2005, *ApJ*, 618, 609
- Mackay, C. D. 1971, *MNRAS*, 154, 209
- Marshall, H. et al. 2001 *ApJ*, 549, L167
- Marshall, H.L., Miller, B.P., Davis, D.S., Perlman, E.S., Wise, M., Canizares, C.R., Harris, D.E., & Biretta, J.A. 2002, *ApJ*, 564, 683
- Marshall, H.L. et al. 2005, *ApJS*, 156, 13
- Marshall, H.L. 2011 *ApJS*, 193, 15
- Massaro, E., et al. 2009a, *A&A*, 495, 691
- Massaro, F., Chiaberge, M., Grandi, P., et al. 2009b, *ApJ*, 692, L123
- Massaro, F., Harris, D. E., Chiaberge M. et al. 2009c, *ApJ*, 696, 980
- Massaro, F., Cheung, C. C., Harris, D. E. 2010a, *AIPC*, 1248, 475
- Massaro, F., et al. 2010b, *ApJ*, 714, 589
- Massaro, F., Cheung, C. C., Harris, D. E. 2011a, *IAUS*, 275, 160
- Massaro, F., Siemiginowska, A., et al. 2011b, in prep.
- Massaro, F., Cheung, C. C., Harris, D. E. 2011c, in prep.
- Meisenheimer, K., Roser, H.-J., Hiltner, P. R., Yates, M. G., Longair, M. S., Chini, R., Perley, R. A. 1989 *A&A*, 219, 63
- Miller, B.P., et al. 2006, *ApJ*, 652, 163
- Miller, B.P., & Brandt, W.N. 2009, *ApJ*, 695, 755
- Orr, M. J. L. & Browne, I. W. A. 1982, *MNRAS*, 200, 1067
- Park, T., Kashyap, V. L.; Siemiginowska, A., van Dyk, D. A., Zezas, A.; Heinke, C. W., Bradford J. 2006 *ApJ*, 652, 610
- Perlman, E.S., Georganopoulos, M., May, E.M., Kazanas, D. 2010a *ApJ*, 708, 1
- Perlman, E.S., Padgett, C.A., Georganopoulos, M., et al. 2010b, *ApJ*, 708, 171
- Pesce, J.E., Sambruna, R.M., Tavecchio, F., Maraschi, L., Cheung, C.C., Urry, C.M. & Scarpa, R. 2001 *ApJL*, 556, L79
- Sambruna, R.M., Maraschi, L., Tavecchio, F., Urry, C.M., Cheung, C.C., Chartas, G., Scarpa, R., & Gambill, J.K. 2002 *ApJ*, 571, 206
- Sambruna, R.M., Gambill, J.K., Maraschi, L., Tavecchio, F., Cerutti, R., Cheung, C.C., Urry, C.M., & Chartas, G. 2004 *ApJ*, 608, 698
- Sambruna, R.M., Donato, D., Tavecchio, F., Maraschi, L., Cheung, C.C., & Urry, C.M. 2007 *ApJ*, 670, 74
- Sambruna, R.M., Donato, D., Cheung, C.C., Tavecchio, F., Maraschi, L. 2008, *ApJ*, 684, 862
- Scarpa, R. & Urry, M. C. 2002 *NewAR*, 46, 405
- Schwartz, D. A., et al. 2000, *ApJ*, 540, L69
- Schwartz, D.A., Marshall, H.L., Lovell, J.E.J., et al. 2006, *ApJL*, 641, L107
- Siemiginowska, A., Bechtold, J., Aldcroft, T.L., Elvis, M., Harris, D. E., & Dobrzycki, A. 2002, *ApJ*, 570, 543
- Siemiginowska, A. et al. 2003 *ApJ*, 595, 643
- Siemiginowska, A., Smith, R. K., Aldcroft, Thomas L., Schwartz, D. A., Paerels, F., Petric, A. O. 2003 *ApJ*, 598L, 15
- Sun, M., Jerius, D., & Jones, C. 2005 *ApJ*, 633, 165
- Tavecchio, F., Maraschi, L., Sambruna, R. M., Urry, C. M. 2000, *ApJ*, 544, L23
- Tavecchio, F., Maraschi, L., Wolter, A., Cheung, C.C., Sambruna, R.M., & Urry, C.M. 2007, *ApJ*, 662, 900
- Taylor, M. B. 2005, *ASP Conf. Ser.*, 347, 29
- Urry, C. M., & Padovani, P. 1995, *PASP*, 107, 803
- Wilson, A.S., Young, A.J., & Shopbell, P.L. 2000 *ApJL*, 544, L27
- Wilson, A.S., Young, A.J., & Shopbell, P.L. 2001 *ApJ*, 547, 740
- Worrall, D.M., Birkinshaw, M., & Hardcastle, M.J. 2001 *MNRAS*, 326, L7
- Worrall, D.M., Birkinshaw, M., & Hardcastle, M.J. 2003 *MNRAS*, 343, 73
- Worrall, D.M., & Birkinshaw, M. 2005, *MNRAS*, 360, 926
- Worrall, D. M. 2009, *A&ARv*, 17, 1
- Wright E. L. 2006, *PASP*, 118, 1711

## APPENDIX

In Tables 7, 8, 9, 10, 11, 12 of this appendix we report: the source name together with the component type and the region size used for the flux measurements, the value of the radio flux densities at given radio frequency, the observed X-ray fluxes in each band (i.e., soft, medium, hard and total, see Section 3 for more details) and the values of the

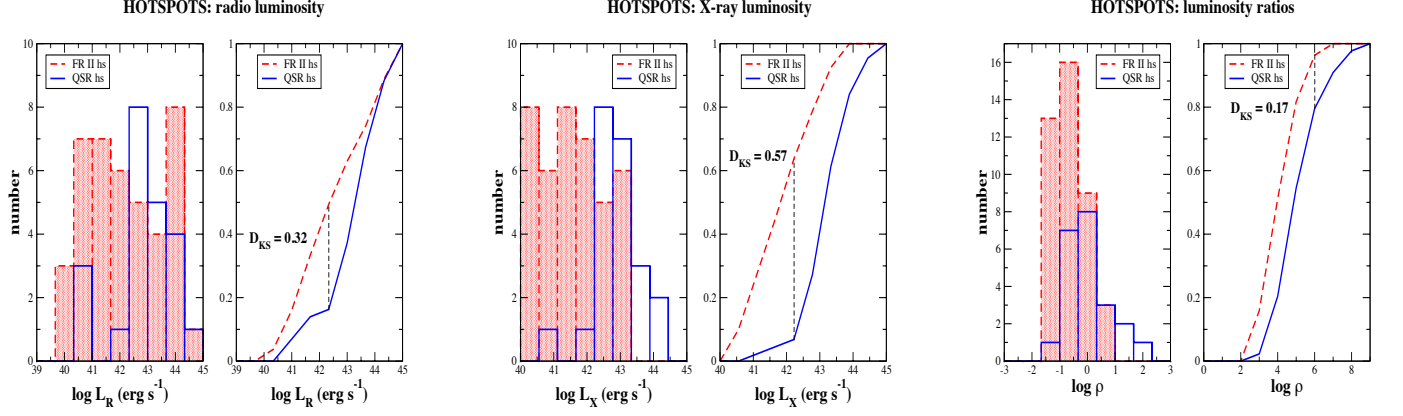


FIG. 17.— a) The distributions of radio luminosities  $L_R$  of hotspots in RGs and QSRs. b) The normalized cumulative distributions of radio luminosities for hotspots in RGs and QSRs. c) The distributions of X-ray luminosities  $L_X$  of hotspots in RGs and QSRs. d) The normalized cumulative distributions of X-ray luminosities for hotspots in RGs and QSRs. e) The distributions of  $\rho$  of hotspots in RGs and QSRs. f) The normalized cumulative distributions of luminosity ratios for hotspots in RGs and QSRs.

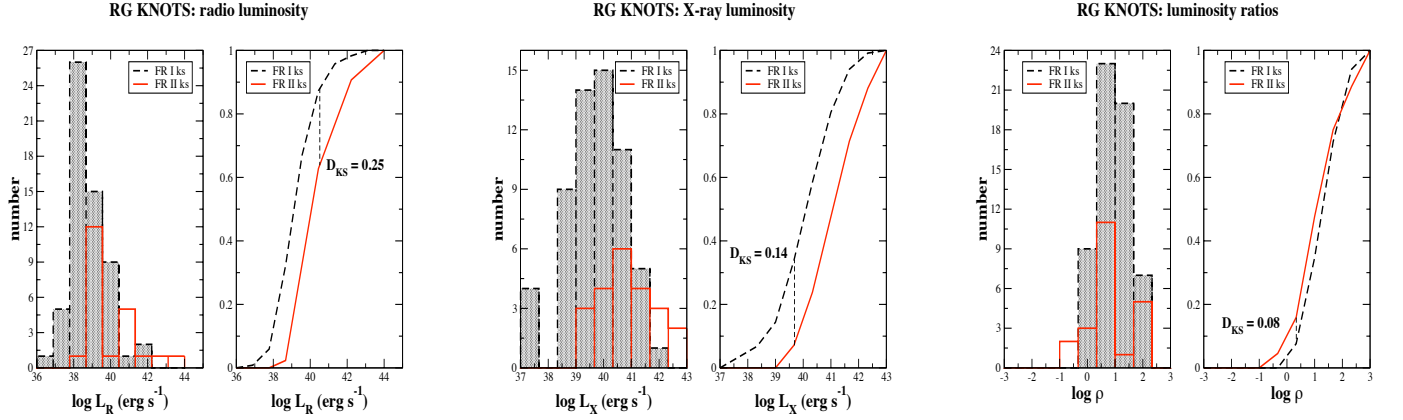


FIG. 18.— a) The distributions of radio luminosities  $L_R$  of knots in RGs. b) The normalized cumulative distributions of radio luminosities for knots in RGs. c) The distributions of X-ray luminosities  $L_X$  of knots in RGs. d) The normalized cumulative distributions of X-ray luminosities for knots in RGs. e) The distributions of  $\rho$  of knots in RGs. f) The normalized cumulative distributions of luminosity ratios for knots in RGs.

ratios corrected for the Galactic absorption (see Section 3.3), for each components in every source of our XJET selected sample. When a dashed line is shown, it implies that the flux is consistent with zero within  $1\sigma$  error.

All the distributions of the observed parameters to compare their properties are shown in Figures 17, 18, 19 20, 21, 22, 23, 24, 25, 26, 27, 28, 29, 30, and 31.

Finally, we also report the distribution of the X-ray count rate for the different components in Figure 32.

TABLE 7

Component	type	region (arcsec)	$\nu_R$ GHz	$S_\nu(\nu_R)$ mJy	$F_{\text{soft}}$ $10^{-15}$ cgs	$F_{\text{med}}$ $10^{-15}$ cgs	$F_{\text{hard}}$ $10^{-15}$ cgs	$F_{\text{tot}}$ $10^{-15}$ cgs	$\rho$
<b>3C 6.1</b>									
n14.0	hs2	c(1.5x1.5)	8.46	255.2	0.26(0.15)	0.54(0.22)	1.68(0.84)	2.48(0.88)	0.14(0.04)
s12.0	hs2	c(2.0x2.0)	8.46	219.5	0.00(0.00)	0.59(0.24)	0.42(0.88)	1.01(0.91)	0.06(0.05)
<b>3C 9</b>									
n5.0	kql	c(1.0x1.0)	8.44	19.1	0.22(0.16)	0.27(0.21)	0.85(0.72)	1.34(0.76)	0.87(0.48)
s7.3	kql	c(1.0x1.0)	8.44	30.5	0.28(0.20)	0.19(0.19)	0.00(0.00)	0.47(0.27)	0.21(0.12)
<b>3C 15</b>									
n4.0	k1	c(1.2x1.2)	8.46	101.5	1.86(0.38)	1.67(0.46)	4.78(1.48)	8.31(1.60)	1.00(0.19)
<b>3C 17</b>									
s3.7	k2	e(0.9x0.6)	4.86	29.9	2.92(1.31)	2.39(0.98)	1.67(1.67)	6.98(2.34)	5.07(1.67)
s11.3	k2	c(0.74x0.74)	4.86	85.3	0.40(0.40)	0.00(0.00)	5.92(3.49)	6.32(3.51)	1.54(0.85)
<b>NGC 315</b>									
n6.3	k1	c(2.0x2.0)	1.43	26.3	2.18(0.68)	4.42(0.59)	3.02(1.07)	9.62(1.40)	28.65(4.15)
n10.5	k1	c(2.0x2.0)	1.43	43.1	3.24(0.49)	3.31(0.47)	4.78(1.31)	11.33(1.47)	20.78(2.53)
n15.3	k1	c(2.0x2.0)	1.43	34.7	2.98(0.45)	3.82(0.49)	4.66(1.18)	11.46(1.35)	25.95(2.89)
<b>3C 31</b>									
n2.1	k1	c(0.8x0.8)	8.46	2.1	4.16(0.59)	5.08(0.67)	4.58(1.25)	13.82(1.53)	86.50(9.09)
n4.2	k1	r(2.95x1.97)	8.46	18.9	3.47(0.54)	3.97(0.62)	3.04(1.09)	10.48(1.37)	7.48(0.92)
n7.0	k1	c(1.2x1.2)	8.46	10.3	0.50(0.22)	1.39(0.34)	2.74(0.82)	4.63(0.92)	5.60(1.09)
<b>0106+013</b>									
s4.4	kqc	c(2.0x2.0)	1.40	468.7	7.98(2.01)	10.2(1.96)	24.9(6.28)	43.08(6.88)	6.77(1.06)
<b>3C 33</b>									
n140.0	hs2	c(3.0x3.0)	4.89	216.1	0.98(0.40)	0.90(0.37)	2.03(2.26)	3.91(2.32)	0.39(0.22)
s112.0	hs2	c(4.0x4.0)	4.89	1076.3	1.11(0.42)	0.36(0.33)	1.35(0.98)	2.82(1.12)	0.06(0.02)
<b>3C 47</b>									
s39.0	hsq	c(2.0x2.0)	4.89	319.0	0.53(0.17)	0.49(0.24)	1.49(0.61)	2.52(0.67)	0.17(0.04)
<b>3C 52</b>									
n34.0	hs2	c(1.2x1.2)	8.44	475.1	0.97(0.69)	1.34(0.77)	0.00(0.00)	2.31(1.03)	0.10(0.05)
<b>4C +35.03</b>									
n3.0	k1	r(4.43x2.46)	4.86	42.4	6.05(1.37)	4.27(1.38)	4.16(3.00)	14.48(3.58)	8.37(1.87)
<b>PKS 0208-512</b>									
s4.0	kqc	c(1.5x1.5)	8.64	33.5	5.10(0.64)	7.25(0.81)	17.90(2.37)	30.25(2.58)	10.70(0.90)
<b>3C 61.1</b>									
s102.0	hs2	c(4.0x4.0)	4.86	465.7	1.27(0.73)	1.14(0.82)	5.01(2.89)	7.42(3.09)	0.36(0.14)
<b>3C 66B</b>									
n2.6	k1	c(1.25x1.25)	8.44	29.2	12.70(0.88)	13.20(1.02)	17.40(2.37)	43.30(2.73)	20.74(1.19)
n5.5	k1	c(1.25x1.25)	8.44	16.8	2.26(0.42)	3.83(0.57)	4.23(1.14)	10.32(1.34)	8.36(1.02)
<b>3C 83.1</b>									
e8.0	k1	c(1.23x1.23)	4.99	6.54	0.03(0.06)	0.32(0.11)	0.51(0.30)	0.86(0.33)	2.90(1.08)
e13.0	k1	c(1.23x1.23)	4.99	5.98	0.11(0.07)	0.07(0.07)	0.24(0.31)	0.43(0.32)	1.90(1.17)
w7.0	k1	c(1.23x1.23)	4.99	2.01	0.14(0.08)	0.14(0.09)	0.53(0.31)	0.81(0.34)	9.96(3.72)
<b>3C 105</b>									
s166.0	k2	c(1.5x1.5)	8.41	40.0	1.81(0.90)	1.83(0.92)	10.10(4.12)	13.74(4.32)	4.64(1.36)
s169.0	hs2	c(1.5x1.5)	8.41	346.5	0.37(0.37)	0.55(0.55)	4.96(2.87)	5.87(2.94)	0.22(0.10)
<b>PKS 0405-123</b>									
n18.7	hsq	c(1.3x1.3)	4.86	197.7	3.59(1.00)	2.92(1.04)	5.13(2.57)	11.64(2.95)	1.31(0.32)
<b>3C 109</b>									
n46.4	hs2	c(1.5x1.5)	8.26	37.9	0.00(0.00)	0.06(0.09)	0.93(0.47)	0.99(0.48)	0.32(0.15)
s48.4	hs2	c(1.5x1.5)	8.26	175.8	0.05(0.05)	0.24(0.14)	0.22(0.22)	0.51(0.27)	0.04(0.02)
<b>PKS 0413-210</b>									
s1.8	kqc	c(1.63x1.63)	4.86	375.8	2.23(1.54)	6.99(2.36)	23.70(7.89)	32.92(8.38)	1.83(0.46)
<b>3C 111</b>									
e9.0	k2	c(1.5x1.5)	1.44	8.6	0.00(0.00)	1.68(1.11)	12.20(5.50)	13.88(5.61)	116.91(45.92)
e15.8	k2	r(5.0x2.5)	1.44	12.9	0.00(0.00)	3.25(1.25)	9.44(4.70)	12.69(4.86)	75.48(27.06)
e29.5	k2	r(4.0x2.5)	1.44	12.9	0.00(0.00)	2.48(1.01)	15.20(4.59)	17.68(4.70)	100.56(25.87)
e43.6	k2	r(4.0x2.5)	1.44	11.0	0.00(0.00)	0.00(0.00)	8.45(3.45)	8.45(3.45)	53.50(21.84)
e60.0	k2	r(6.5x3.0)	1.44	15.2	0.00(0.00)	6.63(1.66)	22.90(6.21)	29.53(6.43)	146.61(30.21)
e98.0	k2	c(2.0x2.0)	1.44	39.6	0.00(0.00)	1.51(0.75)	4.10(2.36)	5.61(2.48)	10.91(4.54)
e121.0	hs2	c(3.0x3.0)	1.44	1771.1	0.51(0.51)	1.67(0.84)	4.20(2.10)	6.38(2.32)	0.34(0.13)

Note: Col. (2) reports the class component accordingly with the definition of Section 2. In Col. (3), where the region size for the flux measurements is shown, the letters ‘c’, ‘r’, and ‘e’ indicate a circular, a rectangular and an elliptical region, respectively. Col. (10) reports the value of the ratios as defined in Section 4.



TABLE 8

Component	type	region (arcsec)	$\nu_R$ GHz	$S_\nu(\nu_R)$ mJy	$F_{\text{soft}}$ $10^{-15}$ cgs	$F_{\text{med}}$ $10^{-15}$ cgs	$F_{\text{hard}}$ $10^{-15}$ cgs	$F_{\text{tot}}$ $10^{-15}$ cgs	$\rho$
<b>3C 120</b>									
w4.0	k1	c(0.74x0.74)	4.86	57.1	0.63(0.22)	2.03(0.39)	14.20(2.21)	16.86(2.25)	6.35(0.82)
w25.0	k1	c(2.0x2.0)	4.86	9.1	0.48(0.15)	2.47(0.39)	31.50(2.97)	34.45(3.00)	79.40(6.81)
<b>3C 123</b>									
e9.0	k2	c(1.5x1.5)	1.49	12593.8	0.82(0.23)	4.76(0.71)	16.20(2.53)	21.78(2.64)	0.12(0.01)
<b>3C 129</b>									
n2.0	k1	c(0.8x0.8)	7.99	1.4	0.00(0.00)	0.44(0.28)	3.03(1.26)	3.47(1.29)	33.45(11.83)
n5.0	k1	c(0.8x0.8)	7.99	2.3	0.00(0.00)	0.32(0.18)	0.52(1.02)	0.84(1.04)	6.22(5.93)
<b>Pictor A</b>									
w250.0	hs2	c(5.0x5.0)	4.87	1709.0	91.8(2.70)	121.0(3.74)	201.00(9.88)	413.80(10.90)	5.21(0.13)
<b>PKS 0521-365</b>									
w1.9	kbl	c(0.8x0.8)	4.86	139.1	21.40(2.65)	27.10(3.67)	27.60(7.76)	76.10(8.98)	12.12(1.37)
e8.6	kbl	c(2.0x2.0)	4.86	1526.7	1.36(0.81)	2.07(1.12)	1.12(1.77)	4.55(2.25)	0.07(0.03)
<b>0529+075</b>									
w2.8	kqc	r(2.0x1.8)	1.40	50.3	1.16(0.67)	3.82(1.21)	12.90(4.60)	17.88(4.80)	29.12(7.27)
<b>PKS 0605-085</b>									
e2.1	kqc	c(0.8x0.8)	4.86	10.4	2.97(1.00)	4.62(1.41)	23.10(6.52)	30.69(6.75)	72.94(14.41)
e4.2	kqc	c(0.8x0.8)	4.86	22.3	3.09(1.03)	4.23(1.30)	19.00(5.28)	26.32(5.53)	29.90(5.67)
<b>3C 173.1</b>									
s31.0	hs2	c(2.5x2.5)	1.48	443.3	0.11(0.11)	0.16(0.16)	1.94(0.97)	2.20(0.99)	0.34(0.15)
<b>3C 179</b>									
w4.5	kql	c(0.8x0.8)	4.87	48.1	0.65(0.46)	1.14(0.66)	0.91(0.91)	2.70(1.21)	1.26(0.55)
w6.5	hsq	c(1.2x1.2)	4.87	69.7	1.18(0.59)	2.79(0.99)	3.18(2.29)	7.15(2.56)	2.25(0.77)
<b>B2 0738+313</b>									
s31.0	hsq	c(2.5x2.5)	4.99	0.83	0.52(0.24)	0.91(0.33)	0.72(0.67)	2.15(0.78)	56.77(19.68)
s36.0	hsq	c(2.5x2.5)	4.99	1.21	0.38(0.19)	0.81(0.33)	0.00(0.00)	1.19(0.38)	22.24(7.09)
<b>3C 189</b>									
e1.3	k1	c(0.5x0.5)	1.66	27.8	3.99(1.33)	5.99(1.63)	11.30(4.39)	21.28(4.87)	49.25(10.86)
<b>0827+243</b>									
s2.6	kqc	c(0.8x0.8)	4.86	0.24	0.47(0.39)	1.74(0.69)	3.70(2.25)	5.91(2.39)	521.17(206.90)
s4.7	kqc	c(0.8x0.8)	4.86	0.54	2.18(0.59)	1.39(0.58)	8.06(2.45)	11.63(2.59)	456.79(99.10)
s5.9	kqc	c(0.8x0.8)	4.86	1.98	0.51(0.30)	0.91(0.47)	0.47(3.08)	4.50(1.49)	48.13(15.68)
<b>4C +29.30</b>									
n11.3	k1	c(1.5x1.5)	4.87	17.5	2.20(0.84)	0.34(0.34)	0.00(0.00)	2.54(0.91)	3.71(1.33)
s17.7	k1	c(1.5x1.5)	4.87	18.2	2.18(0.82)	2.13(0.87)	10.30(4.21)	14.61(4.38)	17.23(4.99)
<b>3C 207</b>									
e4.3	kql	c(1.0x1.0)	8.46	92.5	2.78(0.44)	4.98(0.68)	14.50(2.43)	22.26(2.56)	2.97(0.33)
e6.3	kql	c(1.0x1.0)	8.46	79.0	0.98(0.28)	0.98(0.33)	3.05(1.34)	5.01(1.41)	0.80(0.21)
<b>3C 212</b>									
n5.0	hsq	c(1.0x1.0)	8.46	61.1	0.00(0.00)	0.12(0.28)	0.70(0.70)	0.82(0.75)	0.16(0.15)
s4.7	hsq	c(1.0x1.0)	8.46	166.1	0.00(0.00)	0.64(0.45)	0.00(0.00)	0.64(0.45)	0.05(0.03)
<b>PKS 0903-573</b>									
n2.6	kqc	c(1.0x1.0)	8.64	321.1	0.53(0.84)	5.13(2.14)	4.10(4.10)	9.76(4.70)	0.48(0.22)
<b>3C 219</b>									
s9.3	k2	c(3.0x3.0)	4.56	17.1	0.22(0.25)	0.17(0.44)	3.08(1.74)	3.47(1.81)	4.45(2.32)
s17.6	k2	c(3.0x3.0)	4.56	26.0	0.20(0.26)	0.59(0.41)	5.73(2.87)	6.53(2.91)	5.53(2.46)
<b>PKS 0920-397</b>									
s2.5	kqc	c(1.0x1.0)	8.64	42.0	2.24(0.76)	3.48(1.05)	11.90(3.50)	17.62(3.73)	6.06(1.16)
s4.6	kqc	c(1.0x1.0)	8.64	14.8	1.71(0.61)	2.72(0.79)	1.67(1.21)	6.10(1.57)	7.38(1.72)
s8.6	hsq	c(1.0x1.0)	8.64	50.1	0.19(0.19)	2.07(0.65)	2.13(1.26)	4.39(1.43)	1.20(0.36)
<b>3C 227</b>									
w109.0	hs2	c(2.5x2.5)	1.43	261.6	1.77(0.43)	2.36(0.52)	2.85(1.01)	6.98(1.21)	1.94(0.33)
w117.0	hs2	c(3.0x3.0)	1.43	98.3	0.37(0.21)	0.84(0.32)	3.33(1.27)	4.54(1.33)	3.27(0.95)
<b>Q 0957+561</b>									
e3.5	kql	c(0.8x0.8)	4.86	23.4	0.34(0.17)	0.36(0.20)	1.75(0.73)	2.46(0.77)	2.18(0.68)
<b>4C +13.41</b>									
s9.0	kql	c(2.0x2.0)	8.26	1.6	0.47(0.18)	0.58(0.24)	0.43(0.56)	1.47(0.63)	12.37(5.01)

Note: Col. (2) reports the class component according with the definition of Section 2. In Col. (3), where the region size for the flux measurements is shown, the letters ‘c’, ‘r’, and ‘e’ indicate a circular, a rectangular and an elliptical region, respectively. Col. (10) reports the value of the ratios as defined in Section 4.

TABLE 9

Component	type	region (arcsec)	$\nu_R$ GHz	$S_\nu(\nu_R)$ mJy	$F_{\text{soft}}$ $10^{-15}$ cgs	$F_{\text{med}}$ $10^{-15}$ cgs	$F_{\text{hard}}$ $10^{-15}$ cgs	$F_{\text{tot}}$ $10^{-15}$ cgs	$\rho$
<b>1045-188</b>									
e3.4	kqc	c(1.0x1.0)	1.43	25.3	1.76(0.79)	2.11(0.96)	8.00(3.58)	11.87(3.79)	33.92(10.59)
e5.3	kqc	c(1.0x1.0)	1.43	24.4	0.00(0.00)	2.40(0.98)	0.49(1.11)	2.89(1.48)	8.49(4.30)
e7.3	kqc	c(1.0x1.0)	1.43	78.3	0.60(0.59)	1.40(0.81)	2.73(2.71)	4.73(2.89)	4.36(2.61)
<b>PKS 1046-406</b>									
s3.0	kqc	r(3.43x1.8)	8.64	20.5	5.19(2.36)	3.24(2.36)	8.24(7.17)	16.67(7.91)	11.11(4.76)
<b>4C +20.24</b>									
n4.2	kql	c(1.2x1.2)	1.43	10.9	0.14(0.10)	0.35(0.14)	0.93(0.33)	1.42(0.37)	9.27(2.43)
n11.1	kql	c(1.2x1.2)	1.43	9.1	0.21(0.08)	0.35(0.10)	0.98(0.36)	1.53(0.38)	11.98(2.97)
n14.7	kql	c(1.2x1.2)	1.43	6.3	0.50(0.12)	0.64(0.14)	1.38(0.40)	2.52(0.44)	28.64(4.97)
n18.8	kql	c(1.2x1.2)	1.43	21.8	1.02(0.15)	1.53(0.19)	2.91(0.53)	5.46(0.59)	18.00(1.92)
n21.3	hsq	c(1.2x1.2)	1.43	936.0	1.85(0.20)	2.09(0.22)	2.72(0.52)	6.66(0.60)	0.52(0.05)
<b>3C 254</b>									
w11.8	hsq	c(0.5x0.5)	4.89	154.7	0.39(0.17)	0.19(0.13)	0.26(0.26)	0.84(0.34)	0.12(0.05)
<b>PKS 1127-145</b>									
n3.0	kqc	c(1.2x1.2)	8.46	1.1	2.41(0.33)	2.64(0.41)	7.28(1.42)	12.33(1.51)	138.58(16.43)
n6.5	kqc	c(1.5x1.5)	1.43	2.4	0.87(0.19)	1.32(0.25)	1.82(0.73)	4.01(0.79)	123.08(23.42)
n11.0	kqc	r(5.0x2.0)	8.46	1.3	1.12(0.18)	1.51(0.24)	3.49(0.70)	6.12(0.76)	58.77(7.06)
n19.0	kqc	r(3.0x2.0)	8.46	7.1	0.65(0.14)	0.58(0.14)	1.16(0.48)	2.39(0.52)	4.22(0.88)
n28.0	kqc	c(2.5x2.5)	8.46	13.6	0.31(0.10)	0.36(0.10)	0.66(0.33)	1.33(0.36)	1.22(0.32)
<b>PKS 1136-135</b>									
w4.9	kql	c(1.0x1.0)	4.86	1.4	1.94(0.28)	1.96(0.33)	6.30(1.21)	10.20(1.28)	157.63(19.22)
w7.0	kql	c(1.0x1.0)	4.86	37.3	4.69(0.43)	5.96(0.54)	11.50(1.50)	22.15(1.65)	12.85(0.93)
<b>3C 263</b>									
e16.3	hsq	c(1.5x1.5)	4.86	640.7	2.56(0.35)	2.04(0.35)	4.73(1.20)	9.33(1.30)	0.30(0.04)
<b>3C 264</b>									
n1.8	k1	c(0.5x0.5)	4.95	14.9	2.23(0.76)	0.84(0.81)	2.47(1.82)	5.54(2.13)	7.83(2.93)
<b>3C 265</b>									
e31.0	hs2	c(1.5x1.5)	4.85	313.5	0.47(0.15)	0.28(0.13)	0.85(0.50)	1.59(0.53)	0.11(0.04)
w47.0	hs2	c(1.2x1.2)	4.85	41.7	0.13(0.07)	0.14(0.08)	0.90(0.52)	1.17(0.53)	0.59(0.26)
<b>4C +49.22</b>									
s2.3	kqc	r(1.7x1.2)	4.87	29.6	4.12(1.28)	12.80(2.31)	30.70(7.46)	47.62(7.91)	33.62(5.53)
s4.5	kqc	r(2.5x1.3)	4.87	24.7	2.21(0.93)	4.18(1.26)	5.33(3.47)	11.72(3.81)	10.04(3.19)
s8.0	hsq	r(2.5x1.5)	4.87	47.9	0.80(0.46)	2.20(0.91)	8.32(3.72)	11.32(3.86)	4.92(1.66)
<b>PKS 1202-262</b>									
n2.2	kqc	r(2.5x2.5)	4.86	40.8	8.85(1.07)	15.40(1.48)	52.00(5.37)	76.25(5.67)	41.52(2.95)
n5.5	hsq	c(1.5x1.5)	4.86	48.4	11.30(1.02)	17.70(1.34)	46.80(4.36)	75.80(4.67)	35.42(2.06)
<b>3C 270</b>									
w9.6	k1	c(2.5x2.5)	4.86	4.4	0.00(0.00)	0.09(0.32)	3.33(1.20)	3.42(1.24)	15.85(5.76)
w15.8	k1	c(2.5x2.5)	4.86	7.8	0.84(0.46)	1.46(0.45)	3.42(1.32)	5.72(1.47)	15.49(3.95)
<b>PG 1222-216</b>									
e2.6	kqc	c(0.8x0.8)	4.86	13.8	0.91(0.42)	1.15(0.52)	1.54(2.13)	3.60(2.23)	5.59(3.35)
e4.7	kqc	c(0.8x0.8)	4.86	4.3	0.62(0.31)	0.00(0.00)	0.41(0.92)	1.02(0.97)	5.33(4.76)
n1.0	kqc	c(0.5x0.5)	4.86	60.5	11.10(1.93)	17.30(2.56)	27.80(8.70)	56.20(9.27)	19.74(3.17)
n1.8	kqc	c(0.5x0.5)	4.86	47.8	7.09(1.09)	8.15(1.29)	14.40(3.26)	29.64(3.67)	13.23(1.60)
<b>M 84</b>									
n2.7	k1	c(0.5x0.5)	4.89	3.0	0.39(0.35)	0.04(0.23)	1.04(0.61)	1.47(0.74)	10.40(5.21)
n3.5	k1	c(0.5x0.5)	4.89	10.1	0.33(0.32)	0.47(0.22)	0.49(0.46)	1.29(0.60)	2.76(1.29)
n5.6	k1	c(0.5x0.5)	4.89	11.5	0.35(0.23)	0.00(0.00)	0.47(0.33)	0.81(0.40)	1.56(0.76)
<b>3C 273</b>									
s12.9	kqc	c(1.0x1.0)	1.5	50.3	54.70(2.15)	78.10(2.66)	125.00(6.74)	257.80(7.56)	352.07(10.15)
s15.0	kqc	c(1.0x1.0)	1.5	94.2	41.40(1.85)	41.30(1.94)	77.70(5.21)	160.40(5.86)	117.34(4.20)
s16.8	kqc	c(0.8x0.8)	1.5	95.3	8.78(0.84)	7.96(0.88)	17.60(2.46)	34.34(2.74)	24.79(1.94)
s18.9	kqc	c(0.8x0.8)	1.5	242.9	9.33(0.87)	11.30(1.01)	21.30(2.77)	41.93(3.07)	11.85(0.85)
s20.4	kqc	c(0.8x0.8)	1.5	536.1	8.85(0.85)	11.00(1.01)	11.70(1.96)	31.55(2.36)	4.07(0.30)
<b>PKS 1030-357</b>									
s3.5	kqc	c(1.5x1.5)	8.64	16.7	0.59(0.30)	1.87(0.50)	2.27(1.16)	4.73(1.30)	3.54(0.93)
s6.6	kqc	c(1.5x1.5)	8.64	6.8	0.46(0.32)	1.44(0.44)	1.37(0.81)	3.27(0.97)	6.08(1.76)
s13.3	kqc	c(2.0x2.0)	8.64	29.7	5.01(0.82)	6.74(0.89)	13.60(2.38)	25.35(2.67)	10.8(1.09)
s13.5	kqc	c(2.0x2.0)	8.64	14.8	2.09(0.57)	4.12(0.70)	7.10(1.73)	13.30(1.95)	11.30(1.60)

Note: Col. (2) reports the class component accordingly with the definition of Section 2. In Col. (3), where the region size for the flux measurements is shown, the letters ‘c’, ‘r’, and ‘e’ indicate a circular, a rectangular and an elliptical region, respectively. Col. (10) reports the value of the ratios as defined in Section 4.

TABLE 10

Component	type	region (arcsec)	$\nu_R$ GHz	$S_\nu(\nu_R)$ mJy	$F_{\text{soft}}$ $10^{-15}$ cgs	$F_{\text{med}}$ $10^{-15}$ cgs	$F_{\text{hard}}$ $10^{-15}$ cgs	$F_{\text{tot}}$ $10^{-15}$ cgs	$\rho$
<b>PKS 1030-357</b>									
s3.5	kqc	c(1.5x1.5)	8.64	16.7	0.59(0.30)	1.87(0.50)	2.27(1.16)	4.73(1.30)	3.54(0.93)
s6.6	kqc	c(1.5x1.5)	8.64	6.8	0.46(0.32)	1.44(0.44)	1.37(0.81)	3.27(0.97)	6.08(1.76)
s13.3	kqc	c(2.0x2.0)	8.64	29.7	5.01(0.82)	6.74(0.89)	13.60(2.38)	25.35(2.67)	10.8(1.09)
s13.5	kqc	c(2.0x2.0)	8.64	14.8	2.09(0.57)	4.12(0.70)	7.10(1.73)	13.30(1.95)	11.30(1.60)
<b>M 87</b>									
w0.9	k1	r(2.46x1.23)	4.89	211.8	37.20(1.09)	120.00(2.17)	562.00(8.65)	719.20(8.98)	70.06(0.87)
w2.7	k1	r(2.46x1.23)	4.89	220.6	66.90(1.38)	90.30(1.81)	112.00(3.86)	269.20(4.48)	25.80(0.42)
w3.9	k1	r(1.72x1.18)	4.89	151.2	20.50(0.79)	24.50(1.09)	25.90(2.09)	70.90(2.49)	9.96(0.34)
w6.0	k1	r(2.31x1.23)	4.89	239.5	39.20(1.08)	40.20(1.33)	31.70(2.19)	111.10(2.78)	9.92(0.24)
w8.5	k1	r(1.72x1.23)	4.89	288.3	25.20(0.84)	18.60(0.92)	11.20(1.36)	55.00(1.85)	4.12(0.13)
w9.9	k1	r(0.98x1.23)	4.89	130.1	3.44(0.378)	3.56(0.54)	2.42(0.68)	9.42(0.95)	1.55(0.15)
w10.9	k1	r(0.98x1.23)	4.89	202.5	9.07(0.54)	8.47(0.69)	7.41(1.13)	24.95(1.43)	2.64(0.15)
w12.5	k1	r(2.12x2.12)	4.89	1837.5	173.00(2.10)	180.00(2.48)	189.00(4.87)	542.00(5.85)	6.28(0.07)
w14.4	k1	r(1.72x1.48)	4.89	1093.2	33.40(0.97)	33.40(1.18)	25.70(1.92)	92.50(2.45)	1.81(0.05)
w17.6	k1	r(1.72x1.23)	4.89	850.3	7.63(0.50)	9.18(0.74)	4.17(0.96)	20.98(1.31)	0.53(0.03)
w20.2	k1	e(0.69x0.84)	4.89	240.0	3.35(0.37)	5.22(0.63)	7.73(1.16)	16.30(1.37)	1.43(0.12)
w26.1	k1	e(0.69x0.84)	4.89	166.7	2.01(0.30)	4.12(0.58)	14.20(1.49)	20.33(1.63)	2.53(0.20)
<b>PKS 1229-027</b>									
w2.0	kqc	c(0.8x0.8)	4.75	113.9	3.15(0.85)	5.12(1.18)	9.45(3.49)	17.72(3.78)	3.37(0.70)
<b>3C 275.1</b>									
n3.5	kql	c(1.2x1.2)	8.44	1.4	0.91(0.37)	0.55(0.28)	2.50(1.27)	3.96(1.35)	34.89(11.71)
n9.5	hsq	c(1.2x1.2)	8.44	155.68	2.31(0.49)	2.54(0.59)	6.29(1.76)	11.14(1.92)	0.87(0.15)
<b>3C 280</b>									
e5.0	hs2	c(1.5x1.5)	4.89	339.1	0.40(0.13)	0.41(0.17)	1.17(0.60)	1.98(0.63)	0.12(0.04)
w6.0	k2	c(1.0x1.0)	4.89	46.2	0.04(0.08)	0.10(0.09)	0.74(0.43)	0.88(0.45)	0.39(0.20)
w8.0	hs2	c(1.0x1.0)	4.89	1089.8	0.96(0.19)	0.89(0.23)	1.15(0.59)	3.00(0.66)	0.06(0.01)
<b>1317-520</b>									
e10.0	kqc	c(1.5x1.5)	1.50	41.9	4.49(0.81)	3.23(0.77)	7.86(2.54)	15.58(2.77)	25.46(4.45)
<b>3C 281</b>									
n13.5	kql	c(1.5x1.5)	4.86	18.8	0.52(0.30)	0.00(0.00)	1.60(1.13)	2.12(1.17)	2.32(1.28)
n16.5	hsq	c(1.5x1.5)	4.86	79.0	0.12(0.12)	0.28(0.28)	0.00(0.00)	0.40(0.31)	0.11(0.09)
<b>Centaurus A</b>									
e15.0	k1	c(2.5x2.5)	4.80	315.7	20.40(1.40)	80.10(1.99)	188.00(6.11)	288.50(6.58)	20.30(0.45)
e29.0	k1	c(2.5x2.5)	4.80	262.4	3.24(0.63)	11.30(0.77)	31.80(2.67)	46.34(2.85)	3.91(0.24)
<b>4C +65.15</b>									
s4.5	kql	c(0.8x0.8)	8.46	24.4	0.17(0.12)	0.81(0.29)	0.99(0.57)	1.97(0.65)	0.97(0.32)
w5.0	kql	c(0.8x0.8)	8.46	9.8	0.10(0.10)	0.37(0.19)	0.00(0.00)	0.47(0.21)	0.59(0.26)
<b>3C 287.1</b>									
w65.0	hs2	c(5.0x5.0)	4.86	91.3	1.85(0.92)	1.37(0.97)	4.62(3.27)	7.84(3.53)	1.82(0.80)
<b>Centaurus B</b>									
w3.4	k1	c(1.0x1.0)	8.64	46.2	0.71(0.71)	0.25(0.56)	7.90(4.56)	8.86(4.65)	14.32(12.22)
w5.7	k1	c(1.0x1.0)	8.64	52.1	0.75(0.75)	5.94(2.10)	8.68(6.21)	15.4(6.60)	17.09(11.52)
<b>4C +19.44</b>									
n16.0	hsq	r(2.46x1.72)	4.86	55.4	0.15(0.09)	0.23(0.12)	0.49(0.43)	0.87(0.45)	0.33(0.17)
s4.0	kqc	r(1.54x1.72)	4.86	17.5	0.48(0.20)	0.91(0.30)	1.06(0.89)	2.45(0.96)	3.01(1.15)
s5.3	kqc	r(1.08x1.72)	4.86	7.1	0.04(0.10)	0.29(0.16)	0.00(0.00)	0.33(0.19)	1.02(0.58)
s6.6	kqc	r(1.52x1.48)	4.86	10.8	0.58(0.19)	0.73(0.20)	1.57(0.57)	2.88(0.63)	5.67(1.22)
s8.3	kqc	r(1.87x1.72)	4.86	19.1	0.77(0.20)	0.76(0.22)	1.19(0.58)	2.72(0.65)	3.07(0.71)
s10.0	kqc	r(1.38x1.72)	4.86	6.2	0.29(0.13)	0.58(0.19)	1.26(0.52)	2.13(0.57)	7.24(1.90)
s11.2	kqc	r(1.23x1.72)	4.86	5.4	0.13(0.07)	0.20(0.10)	0.53(0.38)	0.86(0.40)	3.38(1.53)
s12.9	kqc	r(1.87x1.72)	4.86	9.9	0.37(0.16)	1.22(0.25)	1.71(0.66)	3.30(0.72)	7.02(1.51)
s14.6	kqc	r(1.48x1.72)	4.86	9.3	0.59(0.17)	0.77(0.19)	1.19(0.50)	2.55(0.56)	5.92(1.26)
s15.9	kqc	r(1.23x1.72)	4.86	2.8	0.72(0.19)	0.95(0.23)	0.82(0.45)	2.49(0.54)	19.36(4.07)
s17.7	kqc	r(2.46x1.72)	4.86	2.5	1.45(0.27)	1.04(0.25)	2.67(0.78)	5.16(0.86)	44.78(7.27)
s25.7	kqc	c(1.33x1.33)	4.86	3.1	0.49(0.15)	0.25(0.11)	1.82(0.76)	2.56(0.78)	17.02(5.06)
s28.0	hsq	c(1.72x1.72)	4.86	86.1	1.53(0.28)	2.15(0.33)	4.58(1.03)	8.26(1.12)	2.04(0.27)
<b>3C 294</b>									
s9.0	hs2	c(1.0x1.0)	4.82	41.9	0.19(0.07)	0.29(0.09)	0.20(0.20)	0.68(0.23)	0.35(0.11)
n6.0	hs2	c(1.0x1.0)	4.82	170.5	0.11(0.06)	0.14(0.08)	0.43(0.30)	0.68(0.32)	0.08(0.04)

Note: Col. (2) reports the class component accordingly with the definition of Section 2. In Col. (3), where the region size for the flux measurements is shown, the letters 'c', 'r', and 'e' indicate a circular, a rectangular and an elliptical region, respectively. Col. (10) reports the value of the ratios as defined in Section 4.

TABLE 11

Component	type	region (arcsec)	$\nu_R$ GHz	$S_\nu(\nu_R)$ mJy	$F_{\text{soft}}$ $10^{-15}$ cgs	$F_{\text{med}}$ $10^{-15}$ cgs	$F_{\text{hard}}$ $10^{-15}$ cgs	$F_{\text{tot}}$ $10^{-15}$ cgs	$\rho$
<b>3C 295</b>									
n1.9	hs2	c(0.5x0.5)	4.99	2233.4	1.90(0.54)	2.29(0.43)	4.30(1.03)	8.49(1.24)	0.08(0.01)
s2.5	hs2	c(0.5x0.5)	4.99	1987.1	0.90(0.34)	1.55(0.34)	1.98(0.81)	4.43(0.94)	0.05(0.01)
<b>3C 296</b>									
n3.2	k1	c(1.0x1.0)	8.44	2.1	0.24(0.39)	0.87(0.32)	1.21(0.93)	2.32(1.06)	13.28(6.02)
n6.0	k1	c(1.0x1.0)	8.44	4.7	0.18(0.17)	0.78(0.24)	2.58(0.13)	0.97(0.32)	2.56(0.85)
<b>PKS 1421-490</b>									
n5.9	hsq	c(1.0x1.0)	8.64	3088.8	7.66(0.83)	16.10(1.10)	57.70(4.07)	81.46(4.30)	0.36(0.02)
<b>3C 303</b>									
e17.0	k1	c(2.0x2.0)	1.45	5.8	5.53(0.16)	0.45(0.42)	1.05(1.05)	1.50(1.14)	17.79(13.54)
w2.8	k1	c(1.25x1.25)	1.45	24.1	0.95(0.67)	0.00(0.00)	0.00(0.00)	0.95(0.67)	2.98(2.11)
w5.6	k1	c(1.25x1.25)	1.45	22.0	1.14(0.47)	0.73(0.36)	3.52(2.07)	5.39(2.15)	17.26(6.78)
w8.8	k1	c(1.25x1.25)	1.45	17.7	1.58(0.56)	0.95(0.48)	0.00(0.00)	2.53(0.74)	10.54(3.07)
w17.0	k1	c(2.0x2.0)	1.45	745.0	4.25(0.87)	5.90(1.19)	16.60(3.82)	26.75(4.09)	2.53(0.38)
<b>1508+572</b>									
w2.6	kqc	c(1.2x1.2)	1.43	1.3	1.36(0.21)	1.62(0.27)	2.87(0.75)	5.85(0.83)	331.72(45.86)
<b>PKS 1510-089</b>									
s2.4	kqc	r(1.7x1.0)	4.86	11.5	5.10(1.47)	10.20(2.12)	19.40(7.85)	34.70(8.26)	67.99(15.18)
s5.0	kqc	r(2.0x1.7)	4.86	17.0	3.29(1.07)	6.33(1.61)	11.60(5.16)	21.23(5.51)	28.11(6.85)
<b>3C 321</b>									
n147.0	hs2	c(2.0x2.0)	1.51	74.0	0.27(0.14)	0.12(0.12)	0.89(0.52)	1.28(0.55)	1.21(0.50)
s137.0	hs2	c(3.0x3.0)	1.51	489.6	0.42(0.17)	0.33(0.19)	1.88(0.86)	2.64(0.90)	0.38(0.12)
<b>3C 327</b>									
e99.0	hs2	c(5.0x5.0)	8.47	136.3	0.58(0.24)	0.77(0.30)	7.72(1.86)	9.07(1.90)	0.81(0.17)
<b>4C +00.58</b>									
e3.0	k1	c(1.2x1.2)	4.86	43.8	1.21(0.23)	1.28(0.25)	3.44(0.68)	5.93(0.76)	3.10(0.38)
<b>3C 330</b>									
e30.0	hs2	c(2.5x2.5)	8.45	703.7	0.29(0.13)	0.81(0.24)	1.08(0.55)	2.17(0.62)	0.04(0.01)
w32.0	hs2	c(2.5x2.5)	8.45	189.0	0.09(0.06)	0.27(0.13)	0.00(0.00)	0.35(0.15)	0.02(0.01)
<b>NGC 6251</b>									
w6.0	k1	c(1.48x1.48)	1.49	6.5	1.26(0.46)	1.13(0.39)	2.93(1.32)	5.32(1.45)	60.04(15.59)
w9.0	k1	c(1.48x1.48)	1.49	3.4	1.18(0.32)	0.79(0.32)	2.88(1.11)	4.85(1.20)	104.92(24.45)
w15.5	k1	c(1.48x1.48)	1.49	6.5	1.98(0.37)	1.74(0.36)	2.74(0.88)	6.46(1.02)	75.42(11.23)
w20.0	k1	c(1.48x1.48)	1.49	9.3	0.85(0.25)	0.93(0.27)	3.15(1.01)	4.93(1.07)	38.35(8.00)
w23.0	k1	c(1.48x1.48)	1.49	10.9	0.66(0.24)	0.78(0.24)	1.38(0.71)	2.82(0.78)	19.09(5.01)
<b>1642+690</b>									
s2.9	kqc	c(0.9x0.9)	4.86	48.2	2.00(0.83)	2.84(1.30)	16.60(6.42)	21.44(6.60)	9.51(2.84)
<b>3C 345</b>									
n2.8	kqc	c(1.0x1.0)	4.86	241.8	5.80(1.47)	0.31(1.60)	18.70(6.66)	24.81(7.01)	2.15(0.60)
<b>3C 346</b>									
e2.0	k1	c(0.8x0.8)	1.53	538.4	1.39(0.35)	1.07(0.33)	3.37(1.19)	5.83(1.28)	0.77(0.16)
<b>3C 349</b>									
s38.0	hs2	c(2.0x2.0)	1.5	112.4	0.42(0.42)	0.70(0.50)	1.53(1.53)	2.65(1.66)	1.61(0.99)
s43.0	hs2	c(2.0x2.0)	1.5	911.1	0.32(0.32)	1.63(0.81)	1.01(1.01)	2.96(1.34)	0.22(0.10)
<b>3C 351</b>									
n25.0	hsq	c(2.0x2.0)	1.42	548.2	5.84(0.55)	7.23(0.68)	12.50(1.82)	25.57(2.02)	3.39(0.26)
n27.0	hsq	c(2.0x2.0)	1.42	1245.4	4.97(0.50)	6.13(0.62)	8.45(1.59)	19.55(1.78)	1.15(0.10)
<b>3C 353</b>									
e21.0	k2	c(1.2x1.2)	8.44	2.0	0.04(0.06)	0.21(0.11)	0.81(0.57)	1.06(0.58)	6.66(3.53)
e23.0	k2	c(1.2x1.2)	8.44	5.5	0.24(0.12)	0.95(0.22)	1.29(0.53)	2.48(0.59)	5.97(1.34)
e70.0	k2	c(1.5x1.5)	8.44	7.9	0.00(0.00)	0.00(0.00)	1.57(0.73)	1.57(0.73)	2.35(1.10)
e73.0	k2	c(1.5x1.5)	8.44	16.9	0.17(0.10)	0.10(0.07)	0.30(0.34)	0.57(0.36)	0.49(0.27)
e88.0	k2	c(1.5x1.5)	8.44	15.3	0.20(0.11)	0.67(0.20)	1.51(0.65)	2.38(0.69)	2.01(0.55)
w47.0	k2	c(2.0x2.0)	8.44	17.1	0.27(0.12)	0.61(0.19)	2.48(0.77)	3.37(0.80)	2.51(0.57)
<b>4C +62.29</b>									
s1.4	kql	c(0.5x0.5)	4.86	14.4	6.43(1.16)	9.26(1.51)	20.6(4.38)	36.29(4.78)	54.37(6.96)
s2.4	kql	c(0.5x0.5)	4.86	36.1	2.09(0.66)	3.42(0.92)	4.22(2.11)	9.73(2.39)	5.86(1.39)
<b>1800+440</b>									
w3.2	kqc	c(1.3x1.3)	1.51	39.4	5.67(1.67)	9.29(1.93)	14.70(5.32)	29.66(5.90)	52.09(10.11)

Note: Col. (2) reports the class component accordingly with the definition of Section 2. In Col. (3), where the region size for the flux measurements is shown, the letters 'c', 'r', and 'e' indicate a circular, a rectangular and an elliptical region, respectively. Col. (10) reports the value of the ratios as defined in Section 4.

TABLE 12

Component	type	region (arcsec)	$\nu_R$ GHz	$S_\nu(\nu_R)$ mJy	$F_{\text{soft}}$ $10^{-15}$ cgs	$F_{\text{med}}$ $10^{-15}$ cgs	$F_{\text{hard}}$ $10^{-15}$ cgs	$F_{\text{tot}}$ $10^{-15}$ cgs	$\rho$
<b>3C 371</b>									
w1.7	kbl	c(0.7x0.7)	4.86	41.5	25.20(1.65)	29.80(2.10)	34.70(5.87)	89.70(6.45)	48.52(3.28)
w3.1	kbl	c(1.0x1.0)	4.86	98.8	16.30(1.14)	16.80(1.29)	24.20(3.08)	57.30(3.53)	12.99(0.76)
<b>3C 380</b>									
n1.2	kqc	c(0.6x0.6)	1.66	2821.6	36.80(6.03)	52.60(7.90)	84.00(23.00)	173.40(25.06)	4.08(0.55)
<b>3C 390.3</b>									
n103.0	k2	c(2.5x2.5)	1.45	209.8	4.55(0.54)	7.94(0.88)	14.80(2.65)	27.29(2.84)	9.42(0.95)
s87.0	hs2	c(5.0x5.0)	1.45	2786.9	1.42(0.34)	2.86(0.57)	5.49(2.14)	9.77(2.24)	0.25(0.06)
<b>1849+670</b>									
n5.0	kqc	c(1.81.8)	1.40	4.6	1.67(0.75)	1.52(0.89)	0.00(0.00)	3.19(1.16)	58.88(21.07)
<b>4C 73.18</b>									
s2.6	kqc	c(1.0x1.0)	1.43	30.1	4.79(1.53)	8.53(2.32)	0.73(4.45)	14.05(5.25)	39.60(12.97)
<b>3C 403</b>									
e28.0	k2	c(2.0x2.0)	8.47	44.0	1.34(0.30)	2.58(0.43)	4.73(1.20)	8.65(1.31)	2.78(0.38)
e48.0	hs2	c(1.23x1.23)	8.47	13.2	0.40(0.16)	0.60(0.23)	0.84(0.60)	1.83(0.67)	2.08(0.66)
e51.0	hs2	c(1.23x1.23)	8.47	31.0	1.07(0.28)	0.72(0.23)	1.39(0.62)	3.18(0.72)	1.65(0.33)
<b>Cygnus A</b>									
e53.2	hs2	c(1.23x1.23)	4.53	3078.0	0.00(0.00)	0.87(0.54)	3.37(1.91)	4.24(1.98)	0.033(0.01)
e57.7	hs2	c(2.5x2.5)	4.53	59741.4	10.8(0.95)	42.70(2.21)	105.00(6.92)	158.50(7.33)	0.076(0.003)
w63.3	hs2	c(1.48x1.48)	4.53	9109.6	1.28(0.30)	5.43(0.90)	14.90(2.96)	21.61(3.12)	0.067(0.009)
w67.0	hs2	c(2.5x2.5)	4.53	45903.4	8.37(0.82)	27.50(1.76)	76.70(5.79)	112.57(6.11)	0.071(0.003)
<b>2007+777</b>									
w5.0	kbl	c(1.2x1.2)	1.49	2.5	0.30(0.30)	0.74(0.33)	3.86(1.39)	4.90(1.46)	137.67(40.46)
w8.5	kbl	c(1.2x1.2)	1.49	3.0	1.04(0.32)	1.11(0.38)	5.25(1.42)	7.40(1.50)	180.90(34.86)
w11.6	kbl	c(1.2x1.2)	1.49	1.9	0.33(0.20)	0.71(0.29)	1.92(0.98)	2.96(1.03)	114.95(38.02)
<b>PKS 2101-490</b>									
e5.0	kqc	c(1.2x1.2)	8.64	5.6	0.39(0.23)	0.67(0.26)	2.33(0.97)	3.39(1.03)	7.25(2.16)
e8.0	kqc	c(1.2x1.2)	8.64	6.3	0.97(0.33)	0.99(0.28)	1.84(0.75)	3.80(0.87)	7.37(1.64)
e12.0	hsq	c(2.0x2.0)	8.64	46.3	1.26(0.39)	1.80(0.41)	1.86(0.92)	4.92(1.07)	1.30(0.28)
<b>PKS 2153-69</b>									
s26.0	hs2	c(2.5x2.5)	8.64	338.2	2.58(0.73)	3.02(0.88)	1.34(1.34)	6.94(1.76)	0.26(0.06)
n10.3	k2	c(1.0x1.0)	8.64	8.3	0.93(0.42)	2.13(0.75)	1.27(0.90)	4.33(1.25)	6.39(1.80)
n47.0	hs2	c(2.5x2.5)	8.64	89.3	1.04(0.47)	2.10(0.76)	2.32(1.64)	5.46(1.87)	0.74(0.25)
<b>2155-152</b>									
s3.5	kqc	c(1.2x1.2)	1.40	92.1	1.16(0.82)	1.46(1.04)	3.30(2.84)	5.92(3.13)	4.81(2.47)
<b>PKS 2201+044</b>									
n2.2	kqc	c(0.9x0.9)	8.46	15.1	11.90(0.94)	14.20(1.15)	20.60(2.76)	46.70(3.13)	39.44(2.53)
<b>2209+080</b>									
s4.4	kqc	c(1.5x1.5)	4.86	64.1	1.53(0.55)	1.70(0.65)	4.00(1.83)	7.23(2.02)	2.53(0.67)
<b>2216-038</b>									
s8.0	kqc	c(2.0x2.0)	1.40	105.9	0.79(0.57)	2.39(0.99)	7.51(3.82)	10.69(3.99)	7.49(2.72)
s12.4	kqc	c(2.0x2.0)	1.40	39.7	0.00(0.00)	1.50(0.75)	9.67(4.32)	11.17(4.38)	20.3(7.91)
<b>3C 445</b>									
s275.0	hs2	c(9.0x9.0)	1.43	564.7	4.69(0.60)	5.36(0.70)	10.30(2.26)	20.35(2.44)	2.70(0.31)
<b>3C 452</b>									
w130.0	hs2	c(3.0x3.0)	8.47	54.0	0.33(0.13)	0.53(0.16)	0.16(0.35)	1.02(0.41)	0.29(0.10)
<b>3C 454.3</b>									
n2.3	kqc	c(0.8x0.8)	8.46	19.0	5.95(1.25)	7.72(1.55)	10.30(3.98)	23.97(4.45)	16.93(2.91)
w5.4	kqc	c(1.2x1.2)	8.46	138.3	6.94(1.18)	10.60(1.43)	28.60(4.86)	46.14(5.20)	4.28(0.46)
<b>3C 465</b>									
n5.5	k1	c(1.5x1.5)	8.47	5.2	1.76(0.44)	0.75(0.31)	2.07(0.85)	4.58(1.01)	11.79(2.48)
n14.6	k1	c(1.5x1.5)	8.47	2.2	0.17(0.16)	0.20(0.18)	0.24(0.48)	0.61(0.53)	3.62(2.98)

Note: Col. (2) reports the class component accordingly with the definition of Section 2. In Col. (3), where the region size for the flux measurements is shown, the letters ‘c’, ‘r’, and ‘e’ indicate a circular, a rectangular and an elliptical region, respectively. Col. (10) reports the value of the ratios as defined in Section 4.

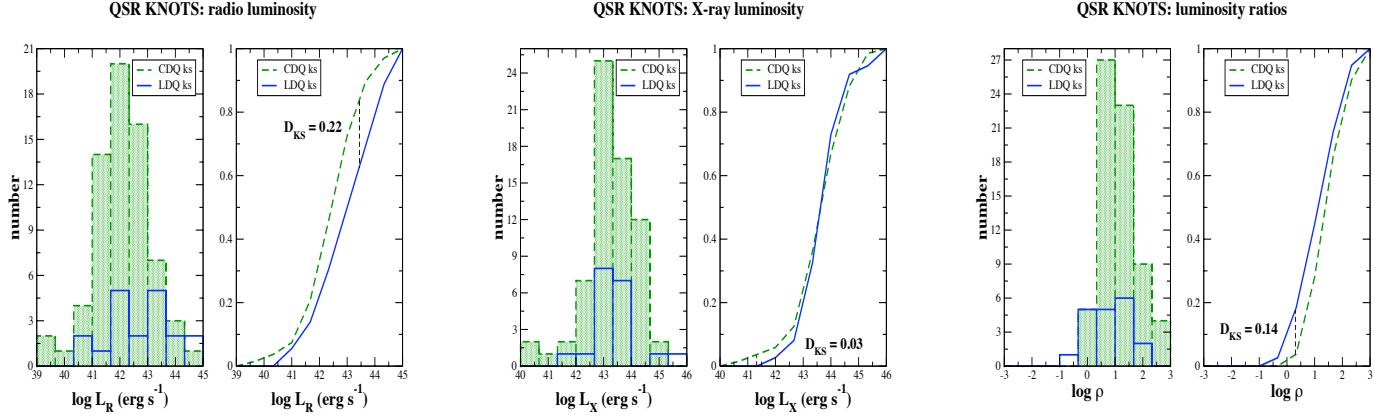


FIG. 19.— a) The distributions of radio luminosities  $L_R$  of knots in QSRs. b) The normalized cumulative distributions of radio luminosities for knots in QSRs. c) The distributions of X-ray luminosities  $L_X$  of knots in QSRs. d) The normalized cumulative distributions of X-ray luminosities for knots in QSRs. e) The distributions of  $\rho$  of knots in QSRs. f) The normalized cumulative distributions of luminosity ratios for knots in QSRs.

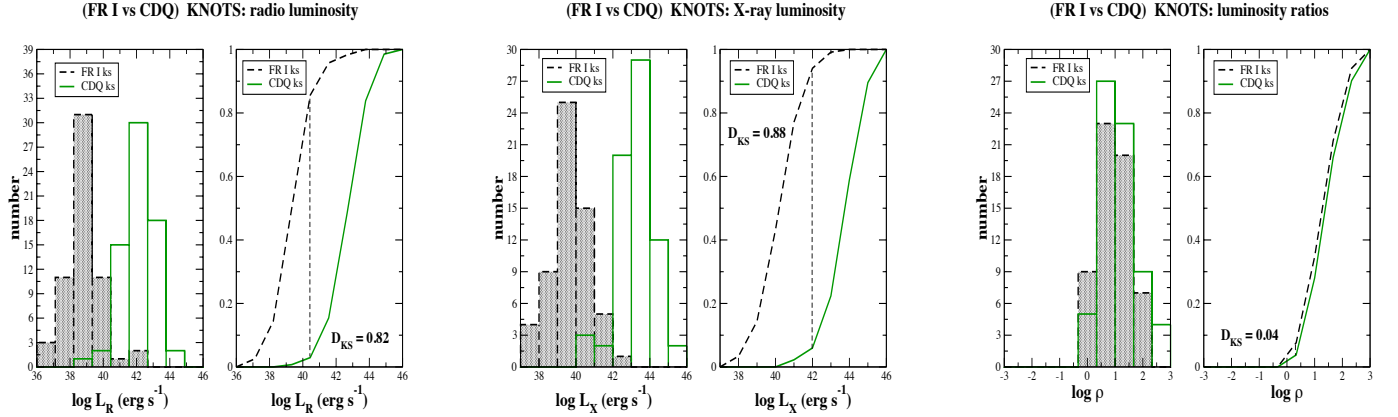


FIG. 20.— a) The distributions of radio luminosities  $L_R$  of knots in FR Is and CDQs. b) The normalized cumulative distributions of radio luminosities for knots in FR Is and CDQs. c) The distributions of X-ray luminosities  $L_X$  of knots in FR Is and CDQs. d) The normalized cumulative distributions of X-ray luminosities for knots in FR Is and CDQs. e) The distributions of  $\rho$  of knots in FR Is and CDQs. f) The normalized cumulative distributions of luminosity ratios for knots in FR Is and CDQs.

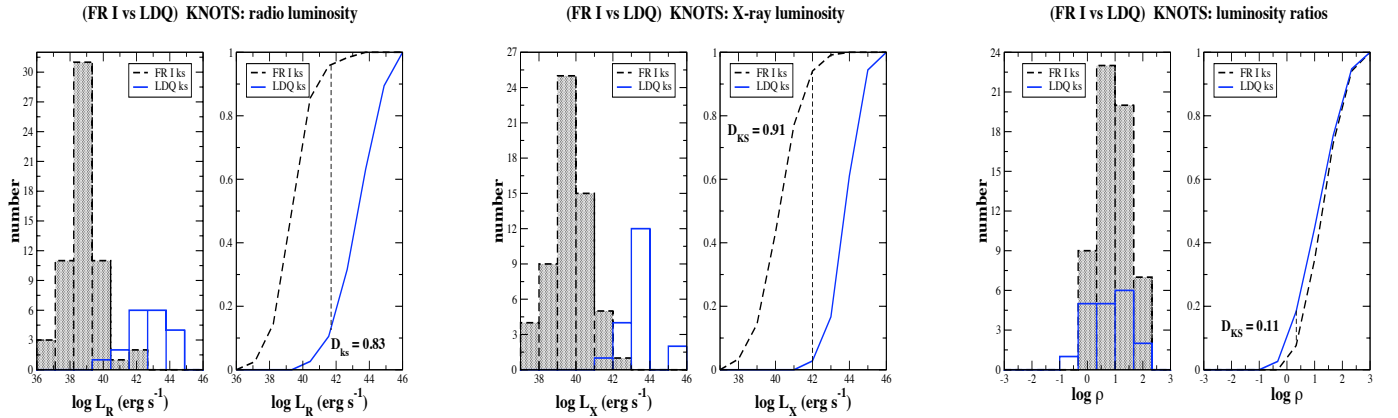


FIG. 21.— a) The distributions of radio luminosities  $L_R$  of knots in FR Is and LDQs. b) The normalized cumulative distributions of radio luminosities for knots in FR Is and LDQs. c) The distributions of X-ray luminosities  $L_X$  of knots in FR Is and LDQs. d) The normalized cumulative distributions of X-ray luminosities for knots in FR Is and LDQs. e) The distributions of  $\rho$  of knots in FR Is and LDQs. f) The normalized cumulative distributions of luminosity ratios for knots in FR Is and LDQs.

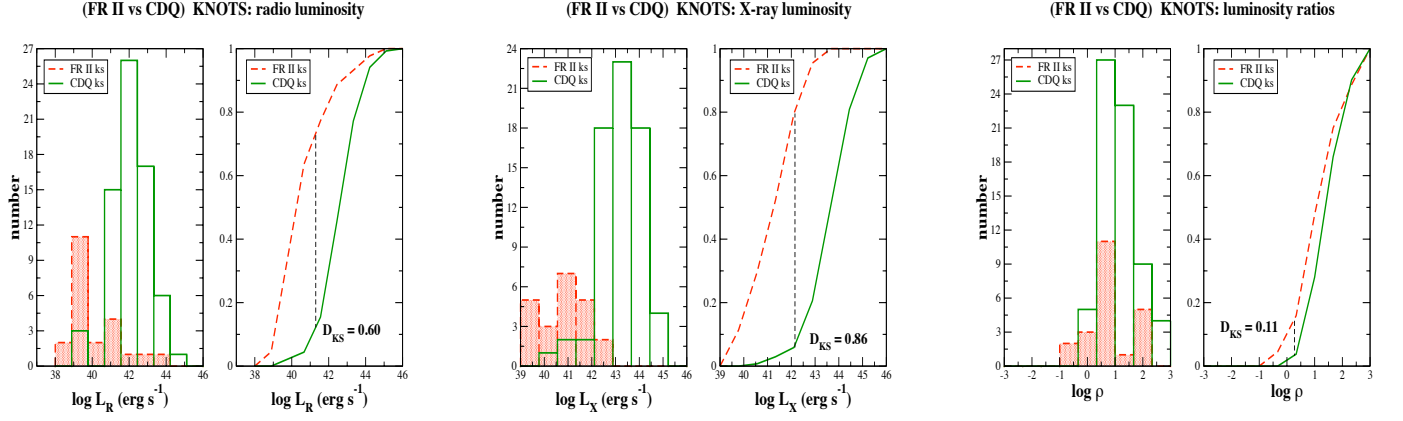


FIG. 22.— a) The distributions of radio luminosities  $L_R$  of knots in FR IIs and CDQs. b) The normalized cumulative distributions of radio luminosities for knots in FR IIs and CDQs. c) The distributions of X-ray luminosities  $L_X$  of knots in FR IIs and CDQs. d) The normalized cumulative distributions of X-ray luminosities for knots in FR IIs and CDQs. e) The distributions of  $\rho$  of knots in FR IIs and CDQs. f) The normalized cumulative distributions of luminosity ratios for knots in FR IIs and CDQs.

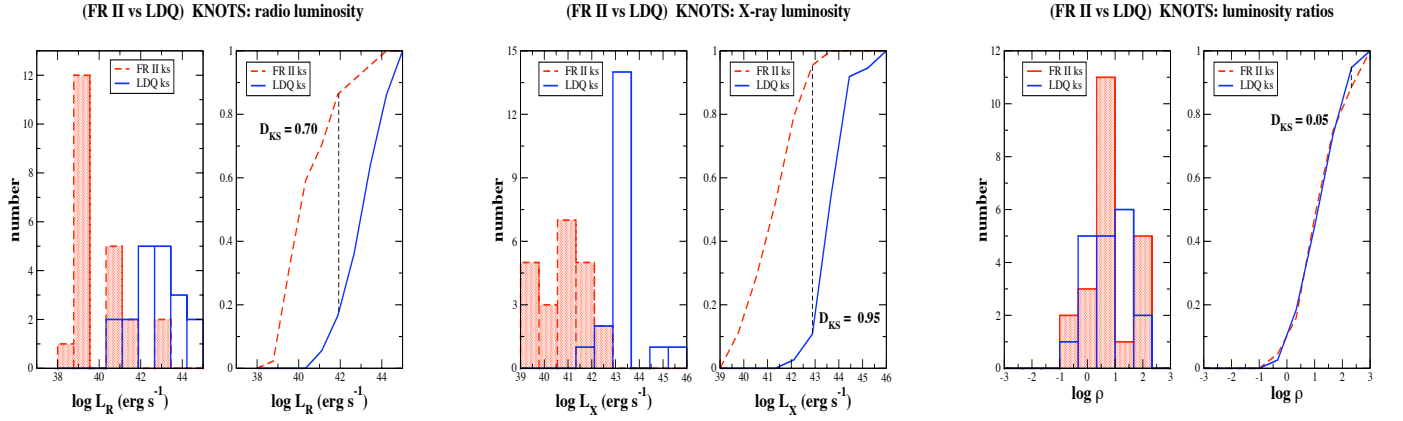


FIG. 23.— a) The distributions of radio luminosities  $L_R$  of knots in FR IIs and LDQs. b) The normalized cumulative distributions of radio luminosities for knots in FR IIs and LDQs. c) The distributions of X-ray luminosities  $L_X$  of knots in FR IIs and LDQs. d) The normalized cumulative distributions of X-ray luminosities for knots in FR IIs and LDQs. e) The distributions of  $\rho$  of knots in FR IIs and LDQs. f) The normalized cumulative distributions of luminosity ratios for knots in FR IIs and LDQs.

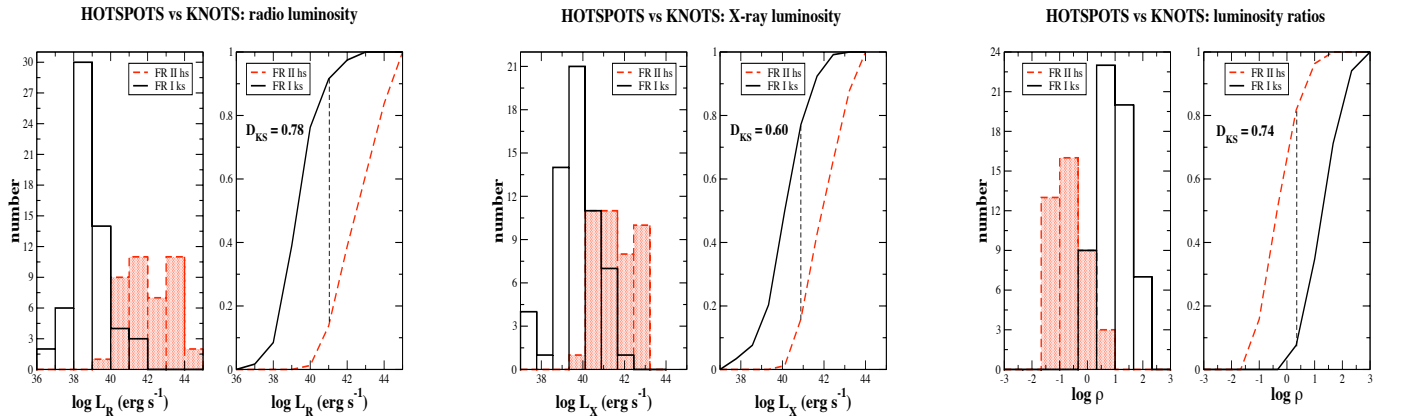


FIG. 24.— a) The distributions of radio luminosities  $L_R$  of hotspots and knots in FR IIs and FR Is. b) The normalized cumulative distributions of radio luminosities for hotspots and knots in FR IIs and FR Is. c) The distributions of X-ray luminosities  $L_X$  of hotspots and knots in FR IIs and FR Is. d) The normalized cumulative distributions of X-ray luminosities for hotspots and knots in FR IIs and FR Is. e) The distributions of  $\rho$  of hotspots and knots in FR IIs and FR Is. f) The normalized cumulative distributions of luminosity ratios for hotspots and knots in FR IIs and FR Is.

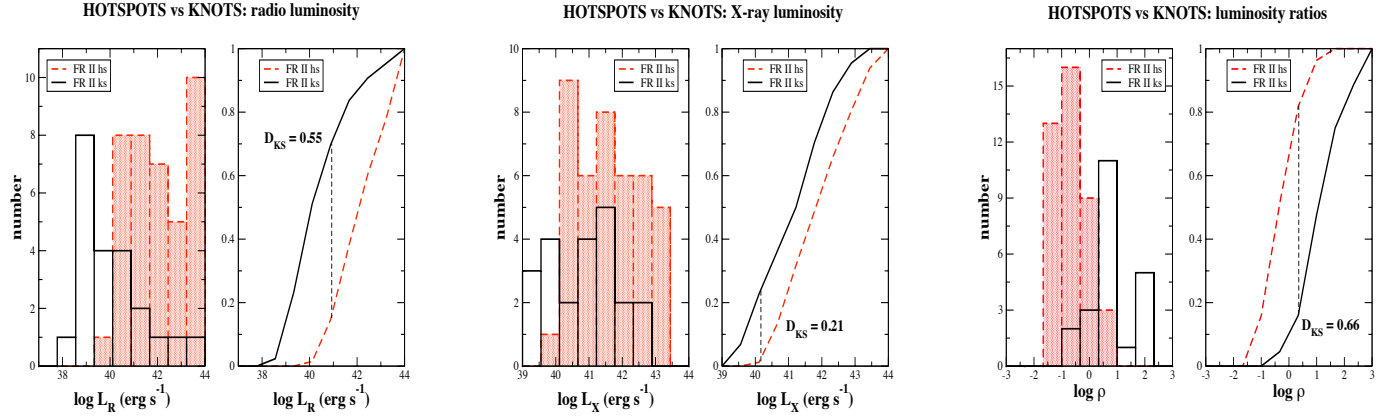


FIG. 25.— a) The distributions of radio luminosities  $L_R$  of hotspots and knots in FR IIs. b) The normalized cumulative distributions of radio luminosities for hotspots and knots in FR IIs. c) The distributions of X-ray luminosities  $L_X$  of hotspots and knots in FR IIs. d) The normalized cumulative distributions of X-ray luminosities for hotspots and knots in FR IIs. e) The distributions of  $\rho$  of hotspots and knots in FR IIs. f) The normalized cumulative distributions of luminosity ratios for hotspots and knots in FR IIs. (Note the different color convention adopted for this figure).

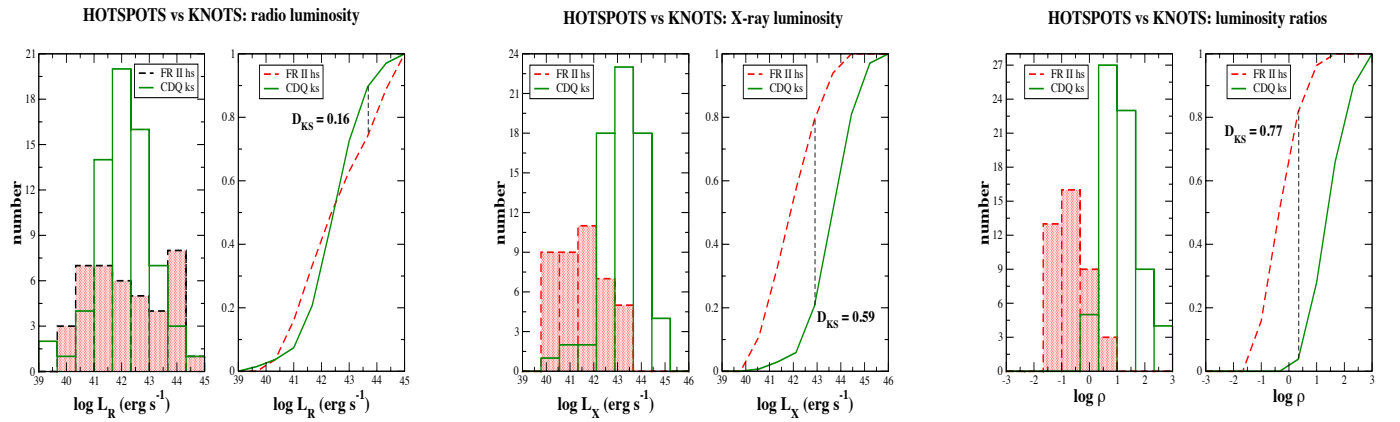


FIG. 26.— a) The distributions of radio luminosities  $L_R$  of hotspots and knots in FR IIs and CDQs. b) The normalized cumulative distributions of radio luminosities for hotspots and knots in FR IIs and CDQs. c) The distributions of X-ray luminosities  $L_X$  of hotspots and knots in FR IIs and CDQs. d) The normalized cumulative distributions of X-ray luminosities for hotspots and knots in FR IIs and CDQs. e) The distributions of  $\rho$  of hotspots and knots in FR IIs and CDQs. f) The normalized cumulative distributions of luminosity ratios for hotspots and knots in FR IIs and CDQs.



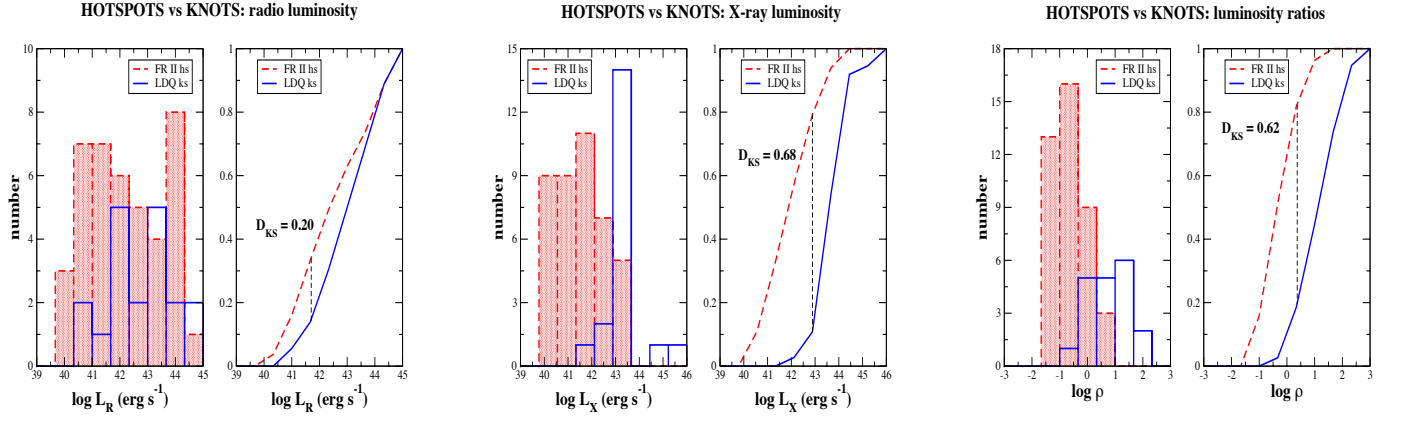


FIG. 27.— a) The distributions of radio luminosities  $L_R$  of hotspots and knots in FR IIs and LDQs. b) The normalized cumulative distributions of radio luminosities for hotspots and knots in FR IIs and LDQs. c) The distributions of X-ray luminosities  $L_X$  of hotspots and knots in FR IIs and LDQs. d) The normalized cumulative distributions of X-ray luminosities for hotspots and knots in FR IIs and LDQs. e) The distributions of  $\rho$  of hotspots and knots in FR IIs and LDQs. f) The normalized cumulative distributions of luminosity ratios for hotspots and knots in FR IIs and LDQs.

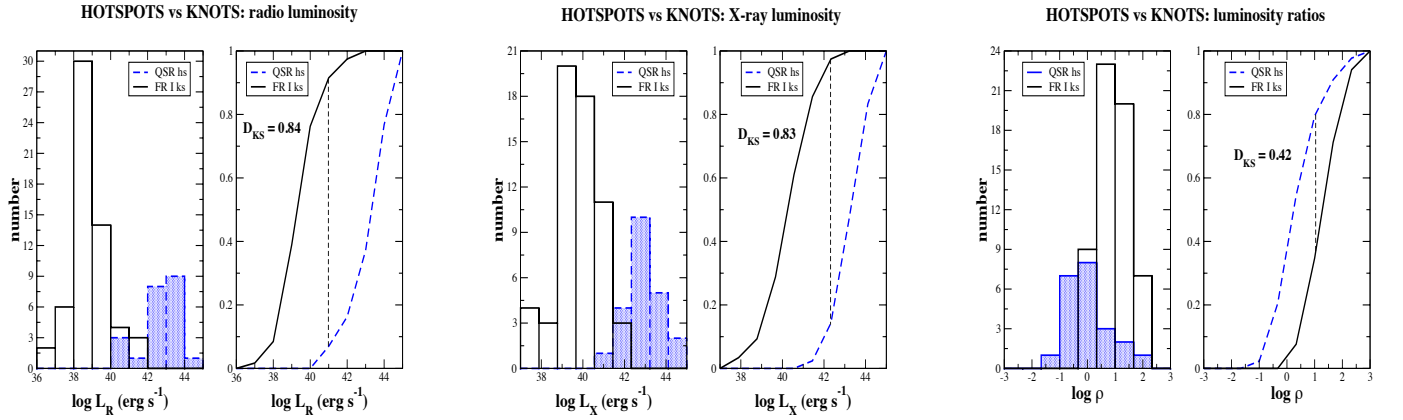


FIG. 28.— a) The distributions of radio luminosities  $L_R$  of hotspots and knots in LDQs and FR Is. b) The normalized cumulative distributions of radio luminosities for hotspots and knots in LDQs and FR Is. c) The distributions of X-ray luminosities  $L_X$  of hotspots and knots in LDQs and FR Is. d) The normalized cumulative distributions of X-ray luminosities for hotspots and knots in LDQs and FR Is. e) The distributions of  $\rho$  of hotspots and knots in LDQs and FR Is. f) The normalized cumulative distributions of luminosity ratios for hotspots and knots in LDQs and FR Is.

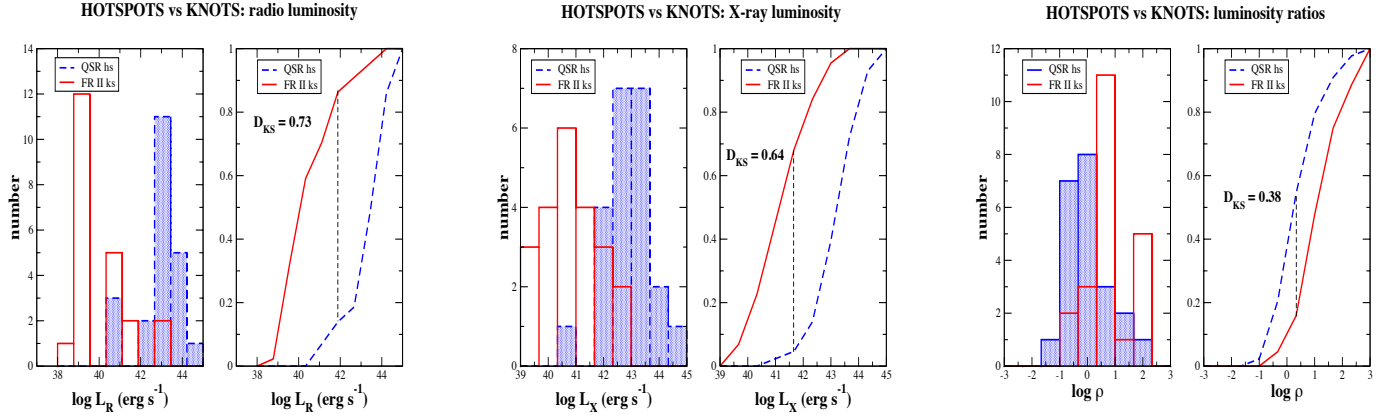


FIG. 29.— a) The distributions of radio luminosities  $L_R$  of hotspots and knots in LDQs and FR IIs. b) The normalized cumulative distributions of radio luminosities for hotspots and knots in LDQs and FR IIs. c) The distributions of X-ray luminosities  $L_X$  of hotspots and knots in LDQs and FR IIs. d) The normalized cumulative distributions of X-ray luminosities for hotspots and knots in LDQs and FR IIs. e) The distributions of  $\rho$  of hotspots and knots in LDQs and FR IIs. f) The normalized cumulative distributions of luminosity ratios for hotspots and knots in LDQs and FR IIs.

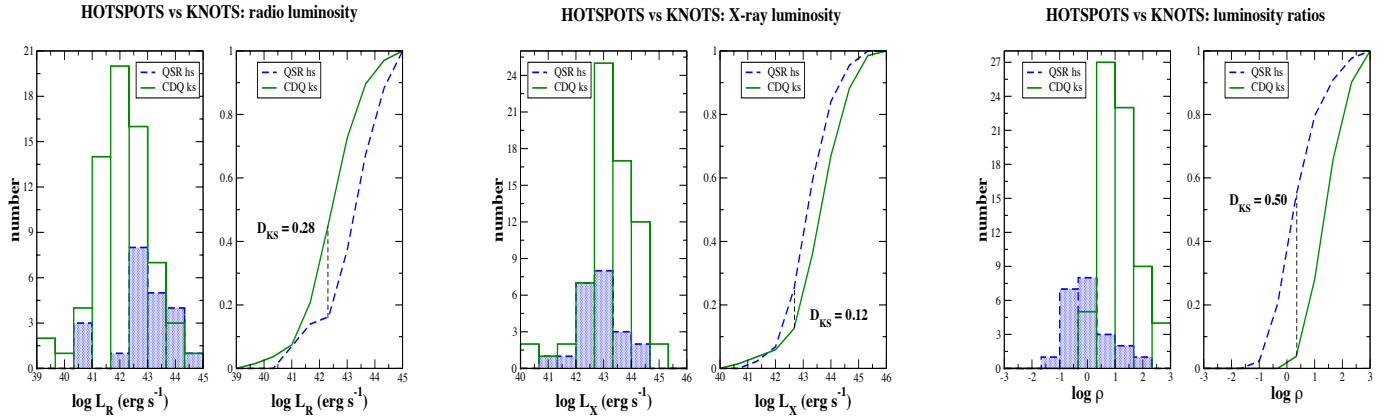


FIG. 30.— a) The distributions of radio luminosities  $L_R$  of hotspots and knots in LDQs and CDQs. b) The normalized cumulative distributions of radio luminosities for hotspots and knots in LDQs and CDQs. c) The distributions of X-ray luminosities  $L_X$  of hotspots and knots in LDQs and CDQs. d) The normalized cumulative distributions of X-ray luminosities for hotspots and knots in LDQs and CDQs. e) The distributions of  $\rho$  of hotspots and knots in LDQs and CDQs. f) The normalized cumulative distributions of luminosity ratios for hotspots and knots in LDQs and CDQs.

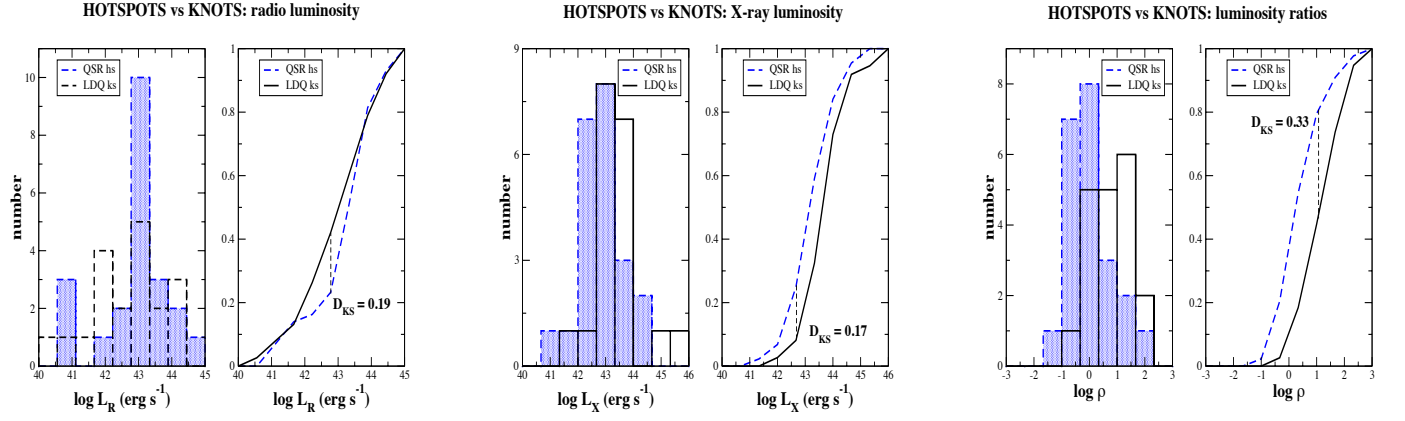


FIG. 31.— a) The distributions of radio luminosities  $L_R$  of hotspots and knots in LDQs. b) The normalized cumulative distributions of radio luminosities for hotspots and knots in LDQs. c) The distributions of X-ray luminosities  $L_X$  of hotspots and knots in LDQs. d) The normalized cumulative distributions of X-ray luminosities for hotspots and knots in LDQs. e) The distributions of  $\rho$  of hotspots and knots in LDQs. f) The normalized cumulative distributions of luminosity ratios for hotspots and knots in LDQs. (Note the different color convention adopted for this figure).

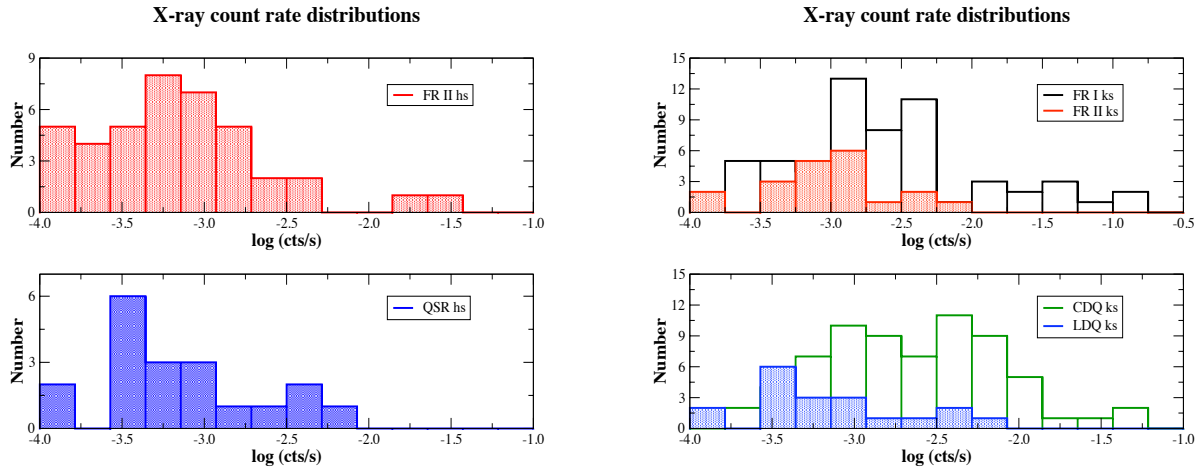


FIG. 32.— The X-ray count rate distribution of hotspots (upper panel) and knots (lower panel).